Antenna Selection and Device Grouping for Spectrum-Efficient UAV-Assisted IoT Systems

Dinh-Thuan Do, *Senior Member, IEEE*, Chi-Bao Le, Alireza Vahid, *Senior Member, IEEE*, and Shahid Mumtaz, *Senior Member, IEEE*

***Abstract*—Unmanned aerial vehicle (UAV)-assisted Internet of Things (IoT) systems have been implemented for over a decade, from transportation to military surveillance, and is proven worthy of integration in the next generation of wireless protocols. Though UAVs have immense potential, they have major drawbacks when it comes to real-world implementation, such as energy capacity, loss of signal quality, and spectrum limitations. To overcome these challenges, integration of UAVs with spectrum-efficient techniques, including cognitive radio (CR) and nonorthogonal multiple access (NOMA) has been proposed. In this article, we incorporate transmit-antenna selection (TAS) into an underlay cognitive radio NOMA network, which provides additional benefits through employing multiple-antenna-selection approach at the UAV with the goal of better serving the ground NOMA devices. The links associated with the multiantenna UAV are theoretically assumed to experience Nakagami-*m* fading distribution. We also emphasize the degraded performance caused by imperfect successive interference cancelation (SIC) when decoding signals at the ground NOMA devices. The closed-form expressions for the proposed model are derived to evaluate two main performance metrics, namely, the outage probability and the ergodic capacity. Monte Carlo simulations are performed to analyze the performance of the system in different scenarios. We observe that the power allocation factors for the devices in a group and the altitude of UAV have a noticeable impact on the performance of the system. Furthermore, the increase in the number of antennas at the UAV can complement these effects and further improve the system performance.**

***Index Terms*—Cognitive radio (CR), imperfect successive interference cancelation (SIC) multiple antenna selection, nonorthogonal multiple access (NOMA), outage probability (OP), unmanned aerial vehicles (UAVs).**

I. Introduction

UMANNED aerial vehicle (UAV) is an emerging technology that has an immense capacity to benefit applications, such as military surveillance, network coverage, and transportation. Since UAV systems possess capabilities, such as extensive coverage, easy deployment for robust and reliable communications in critical scenarios, UAV communications have become a trending topic in the research community [1], [2], [3]. UAVs have the advantage of acting as a flying base station (BS) in many real-world applications; thereby providing Line-of-Sight (LoS) communications to the users on the ground and establishing an air-to-ground (A2G) link [4]. Recently, nonorthogonal multiple access (NOMA) has proven to be one of the most efficient communication techniques in multiple access technique evolution [5]. NOMA-assisted systems can simultaneously allocate the same spectrum resource to two users. This feature enables massive device connectivity and enhanced spectrum utilization during communication. NOMA superimposes the two users' signals during the initial transmission from the sender and transmits them to the receivers. On the receiver side, the successive interference cancelation (SIC) technique is performed to retrieve the desired messages from the superimposed signal. Resource allocation in the system is varied based on power allocation to the users, which depends on the channel state information (CSI) of each user [6]. Shi et al. [7] introduced UAV-aided NOMA with full-duplex capability as a new way to enhance spectrum efficiency. Therefore, NOMA has been highly recommended to be implemented in integrating UAV systems in the beyond fifth-generation (5G) and sixth-generation (6G) communications because of its improved spectrum efficiency and massive device connectivity. Significant research attempts were also performed to analyze the NOMA users' performance with the addition of UAVs. However, spectrum scarcity has become a major bottleneck in applications such as the Internet of Things (IoT) and vehicular networks, and must be addressed.

A. Related Studies

For the past two decades, the cognitive radio (CR) network technology has been developed and tested to address spectrum scarcity in mobile applications. Several studies explored integrating UAVs with CR. For example, UAV-based CR was proposed in [8], [9], [10], [11], [12], [13], and [14] to improve the spectrum sensing capability of the system. Sboui et al. [9] have proposed a power allocation framework to enhance the energy efficiency of the UAV-based cognitive systems. The results demonstrated the role of altitude in minimizing power

Manuscript received 25 July 2022; revised 3 November 2022; accepted 9 December 2022. Date of publication 15 December 2022; date of current version 25 April 2023. The work of Dinh-Thuan Do and Alireza Vahid was supported in part by NSF under Grant ECCS-2030285, Grant CNS-2106692, and Grant CNS-2211804. *(Corresponding author: Alireza Vahid.)*

Dinh-Thuan Do and Alireza Vahid are with the Electrical Engineering Department, University of Colorado Denver, Denver, CO 80204 USA (e-mail: thuandinh.do@ucdenver.edu; alireza.vahid@ucdenver.edu).

Chi-Bao Le is with the Faculty of Electronics Technology, Industrial University of Ho Chi Minh City, Ho Chi Minh City 700000, Vietnam (e-mail: lechibao@iuh.edu.vn).

Shahid Mumtaz is with the Department of Applied Informatics, Silesian University of Technology, 44-100 Gliwice, Poland, and also with the Engineering Department, Nottingham Trent University, NG1 4FQ Nottingham, U.K. (e-mail: dr.shahid.mumtaz@ieee.org).

Digital Object Identifier 10.1109/JIOT.2022.3229592

consumption. Zheng et al. [10] considered the physical-layer security (PLS) of UAV-based CR systems, and concluded that the secrecy rate of the proposed system is significantly enhanced by robustly adjusting the transmit power of the UAV. Pan et al. [11] have studied the UAV-based overlay CR network, where a UAV is present in the secondary network (SN) and an efficient solution was proposed for minimizing energy consumption. Hu et al. [12] have proposed a UAV-based CR and aimed to identify the optimal position of the UAV to provide maximized sensing performance and data rate while protecting the secrecy of the primary network (PN) users. UAV-assisted jamming wideband CR was considered in [13] to enhance the secure transmission in the SN. The UAV sends a jamming signal to the eavesdropper; while the secondary BS continues to provide its services to its users. This approach maximizes of the total average secrecy rate of the SN. Similarly, He et al. [14] considered a CR-aided UAV system to enhance network security by employing artificial noise embedded in transmit signals. The spectrum sensing time, the power splitting ratio, and the hovering position of the UAV are jointly optimized to maximize the total secrecy rate of primary and secondary users.

An NOMA-assisted UAV system was proposed in [15] and the main results are the analytical expressions of the connection outage probability (OP), secrecy OP, and effective secrecy throughput. NOMA-assisted spectrum-efficient systems were proposed in [16] and [17] by comprehensively evaluating the system performance. Singh and Upadhyay [17] derived the OP expressions for the primary and SNs when the full-duplex-based energy harvesting benefits were incorporated. The proposed system's performance was studied in terms of OP and ergodic capacity (EC). NOMA underlaying UAV was proposed in [18] where joint time allocation and power control algorithms are designed for efficient energy utilization in the system. Cooperative and cognitive radio NOMA (CRNOMA) in assistance with UAV was proposed in [19] to study the user fairness in the SN at hot-spot locations. Depending on the UAV location, the authors proposed a methodology to determine the user clustering and channel assignment based on available optimal resources. However, there remains a need for a deeper understanding of the performance of UAV-assisted systems with high spectrum efficiency, which would be suitable for deployment to support a large number of distributed IoT ground devices with applications in health monitoring, traffic flow, and wireless sensors for smart cities.

B. Motivations and Our Contributions

Despite all the recent efforts, there is a significant amount of work to be done in order to enable spectrum-efficient massive connectivity, which is essential in the integration of CR with UAV and NOMA techniques designed for cognitive IoT applications. The work in [15] only considered a single-antenna UAV; while the advantages of multiple-antenna UAVs were not investigated. Incorporating multiple-antenna UAV enables the great benefits of multiantenna architectures in UAV-assisted systems. On the other hand, we extend the system model of [8] by incorporating a UAV. The recent work in [19] studied CRNOMA networks and derived closed-form expressions to obtain the optimal power and time allocations for generic cluster sizes, but the main analysis of performance metrics is missing. Different from [8], [15], and [19], we target to provide a complete mathematical analysis of system performance metrics for the UAV CRNOMA-inspired IoT system. To improve the spectrum efficiency, IoT devices may adopt NOMA device grouping [20], which enables simultaneous transmissions to a pair of secondary devices using the same frequency. The different performance of the two devices was not addressed in [20] and [21], which motivates us to investigate the performance gap between the two devices. Moreover, to further improve the spectrum efficiency, we consider an underlay UAV-aided CR in the presence of NOMA, where multiple-antenna UAVs are deployed to assist the communication between the devices through added diversity. The multiple-antenna UAV design brings the advantages of multiantenna technology to these new systems. Especially, we focus on the performance analysis of a dedicated group of devices, i.e., the primary device (PD) in the primary and the two devices in a specific group of the SN.[1] As far as the authors are aware, the technical literature lacks results that provide a complete analysis of the system performance metrics with complex design, especially in the context of CRNOMA with multiantenna UAV. The main contributions are as follows.

1) We investigate and analyze the performance of an UAV CRNOMA-inspired IoT system over Nakagami-m fading channels with perfect and imperfect SIC to understand how they affect the system performance. In this system, the SN deploys a multiple-antenna UAV to better serve the IoT devices and protect the PDs' spectrum access.
2) Under perfect SIC (pSIC) and imperfect SIC (ipSIC) cases, the expressions of the OP and the EC are derived. More importantly, we identify the main parameters to adjust system performance as expected, for example the number of transmit antennas at the UAV, and the levels of ipSIC. Further, we present a low-complexity algorithm to achieve the optimal outage behavior at the IoT users.
3) Detailed performance comparisons of the UAV-based CRNOMA system are conducted to confirm the superiority of the NOMA scheme in terms of outage behavior as well as ergodic performance. We observe that the optimal OP of the near device can be achieved if we allocate 35% of the transmit power to it, while the EC of the far device meets saturation when the transmit signal-to-noise ratio (SNR) at the UAV is greater than 30 dB.

The remaining sections of this article are organized as follows. Section II describes the system and channel models. Sections III and IV provide the outage probabilities and

[1]The device grouping scheme is based on the ordered channel gains of IoT devices. The nonorthogonally scheduled IoT devices in each group, including the near and far devices form an NOMA two-device in the same channel. We note that each group occupies a channel orthogonal to those occupied by the other groups. The details of device grouping in clustering NOMA approach can be referred in [20].

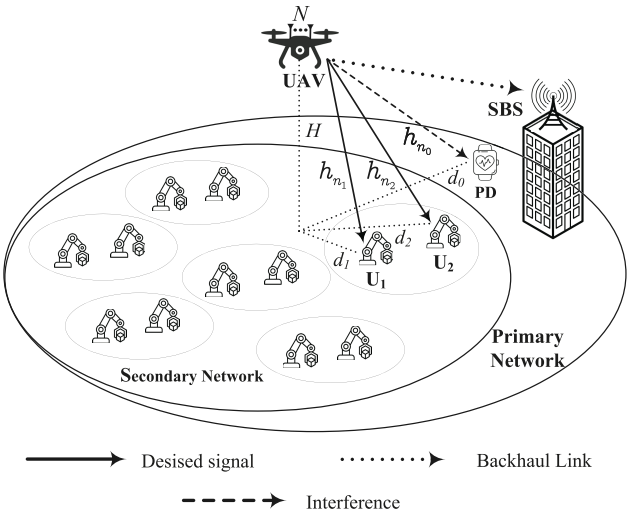

Fig. 1. Illustration of UAV-assisted NOMA systems for cognitive IoT applications.

the asymptotic expressions of the secondary devices, respectively. The EC analyses are presented in Section V. Section VI includes the numerical evaluation of the performance. Finally, the main findings are concluded in Section VII.

II. System Model and Channel Characteristics

A. System Description

An SN in cognitive IoT applications may have several subsets of devices, which are served by the secondary multiple-antenna transmitter (a UAV in our model)[2] as shown in Fig. 1. As various wireless networks, e.g., small-cell network, macrocell network, Wi-Fi, and picocell network, need to coexist in the future, the demand for spectrum resources keeps increasing. As a promising application, the system described above is applicable to the industrial IoT and allows the SN to share the spectrum. We focus on a cognitive SN where devices use the same spectrum resources opportunistically and need performance improvements. A set of all secondary IoT devices is divided into several subsets. The system needs a common reliable control channel to exchange spectral sensing information and the resource allocation. We assume the CSI is known globally, which is common in existing works [12], [22], [23].[3] In the uplink transmission, each BS can estimate the CSI for each secondary IoT device, and then, the BS feeds this information back to each corresponding secondary IoT device.[4] These links are assumed to follow Nakagami-*m* fading distribution [22], [23].[5] We provide the notations of the main parameters in Table I. The Euclidean distances from UAV to the receivers are denoted by d_k, $k \in \{\text{PD}, U_1, U_2\}$, and expressed as follows:

$$d_k = \sqrt{d_i^2 + H^2}, i \in \{0, 1, 2\} \tag{1}$$

where d_i's are the distances from PD, U_1, U_2 to the center point.

1) Signal Processing at Transceivers: In this article, we consider an underlay cognitive system where the secondary transmitter must obey a transmit power constraint [30] given by

$$P_A = \min\left(\bar{P}_A, \frac{Q}{\max_{n_0=1,\ldots,N} |h_{n_0}|^2}\right) = \min\left(\bar{P}_A, \frac{Q}{|h_{n_0^*}|^2}\right) \tag{2}$$

where $\bar{P}_A$ is the maximum power of the secondary transmitter, and Q is the interference temperature constraint (ITC) at PD. The goal of the transmit-antenna selection (TAS) is to find the index of the best transmit antenna that achieves the maximum sum of the squared channel gains between the UAV and the ground users. The CSI feedback signal from the ground users to the UAV assists this selection. The best antenna (the index of the best antenna) for each direction can be selected according to [32]

$$n_0^* = \arg \max_{n_0=1,\ldots,N} |h_{n_0}|^2 \tag{3a}$$

$$n_1^* = \arg \max_{n_1=1,\ldots,N} |h_{n_1}|^2 \tag{3b}$$

TABLE I
Notation for the Main Parameters

Symbol	Notation
$\bar{x}_i$	Signal at User i, $i \in \{1, 2\}$
a_i	Power allocation coefficients at User i
n	$n \in (1, 2, ..., N)$ index of transmit antenna
R_i	Target rate at User i
$\bar{\omega}_{U_i}$	The AWGN noise term followed $\mathcal{CN}(0, N_0)$
P_A	The transmit power at UAV
$\bar{P}_A$	The maximum power of the secondary transmitter
Q	The peak interference power of PD
H	The vertical height of the UAV
d_{PD}	Distance from UAV to PD
d_{U_1}	Distance from UAV to U_1
d_{U_2}	Distance from UAV to U_2
α	Path loss exponent
h_{n_0}	Channel gain from UAV to PD
h_{n_1}	Channel gain from UAV to U_1
h_{n_2}	Channel gain from UAV to U_2

[2]This operation of UAV-aided system is adopted similar to [7]. The fly-hover communication protocol is implemented to assist the UAV to serve data transfer to the ground devices.

[3]As a future direction, it would be interesting to see how the results change when the perfect CSI assumption is replaced with delayed [24], [25], local [26], [27], [28], and intermittent [29] knowledge.

[4]It is worth noting that we focus on the performance analysis of a dedicated device group within an IoT system, which would work with a small coverage area. In this article, UAV acts as a flying BS dedicated to serve targeted IoT devices. Therefore, our model is reasonable to deploy for a single UAV. Besides, the multiple UAV-assisted relays selected with secrecy capacity maximization criteria under CR was proposed and investigated in detail [30].

[5]We note that the distributions of the Nonline-of-Sight (NLoS) and LoS components affect the performance of the considered system. In particular, the Nakagami fading parameter m indicates LoS and NLoS scenarios, i.e., $m = 1$ for NLoS scenario (Rayleigh fading case) and LoS scenario corresponds to case of $m > 1$ [31]. According to the experimental results, Nakagami-*m* distribution is more suitable to characterize the channels when UAVs are placed at low-altitude positions.

$$n_2^* = \arg \max_{n_2=1,\ldots,N} |h_{n_2}|^2. \tag{3c}$$

With respect to retaining the quality of the received signal at each device in a dedicated group of devices, the UAV communicates to two ground single-antenna NOMA devices, i.e., U_1 and U_2, in spectrum sharing scenario with the PN and the presence of a primary receiver (denoted as PD), shown in Fig. 1.[6] The received signals at the destinations are

$$\bar{y}_{U_1} = h_{n_1}\left(\sqrt{a_1 P_A}\bar{x}_1 + \sqrt{a_2 P_A}\bar{x}_2\right) + \bar{\omega}_{U_1} \tag{4a}$$

$$\bar{y}_{U_2} = h_{n_2}\left(\sqrt{a_1 P_A}\bar{x}_1 + \sqrt{a_2 P_A}\bar{x}_2\right) + \bar{\omega}_{U_2} \tag{4b}$$

where $\bar{\omega}_{U_i} \sim \mathcal{CN}(0, N_0)$, $i \in \{1, 2\}$ denotes the additive white Gaussian noise (AWGN) with zero-mean and variance N_0. Following the principle of NOMA, the device U_1 is considered as the near device, which is allocated less power compared with the far device U_2. In the following section, we present details on signal-to-interference-plus-noise ratio (SINR) calculations used to evaluate the received signals and the related system performance metrics.

2) SINR Computation: From (4a), since the NOMA scheme is adopted,[7] i.e., U_1 first decodes the information intended for U_2, $\bar{x}_2$, by treating $\bar{x}_1$ as the interference signal (IS). Hence, the received SINR at U_1 to detect $\bar{x}_2$ is given by

$$\bar{\Gamma}^*_{U_1,\bar{x}_2} = \frac{P_A a_2 \left|h_{n_1^*}\right|^2}{P_A a_1 \left|h_{n_1^*}\right|^2 + N_0} = \frac{\rho_A a_2 \left|h_{n_1^*}\right|^2}{\rho_A a_1 \left|h_{n_1^*}\right|^2 + 1} \tag{5}$$

where $\rho_A = P_A/N_0$ is the SNR at the source. Note that $\bar{x}_1$ and $\bar{x}_2$ are supposed to be normalized unit-power signals, i.e., $\mathbb{E}\{|\bar{x}_1|^2\} = \mathbb{E}\{|\bar{x}_2|^2\} = 1$ in which $\mathbb{E}\{\cdot\}$ denotes expectation operation.

In practice, it is difficult to achieve pSIC, resulting in residual interference while detecting $\bar{x}_1$. Hence, the SINRs at U_1 for the detection of $\bar{x}_1$ can be represented, respectively, as

$$\bar{\Gamma}^{*,\text{ipSIC}}_{U_1,\bar{x}_1} = \frac{\rho_A a_1 \left|h_{n_1^*}\right|^2}{\rho_A |g_I|^2 + 1} \tag{6a}$$

$$\bar{\Gamma}^{*,\text{pSIC}}_{U_1,\bar{x}_1} = \rho_A a_1 \left|h_{n_1^*}\right|^2 \tag{6b}$$

[6]The development of a smaller cluster associated with the two paired devices served by UAV-mounted BS achieves lower decoding complexity, less interference and shorter delay at the receivers compared to multidevice cluster NOMA [20]. If the number of devices in the network is very large, the number of UAVs must also increase, leading to higher cost. It is worth noting that two-user model keeps reducing delay since less procedures of signal detection sent from ground users to the UAV. The situation of more users located in a cluster leads to worse performance at users since much interference exists among those users. Additionally, such flying UAV-mounted BS forms a connected graph with some nearby stationary BSs (SBSs) equipped powered signal processing units, which can proceed with multidevice scenarios rather than UAV-mounted BS. The reliable connection for backhaul from SBSs UAV-mounted BS is assumed perfect and its analytical details along with the clustering problem are beyond the scope of this article.

[7]By employing device grouping with NOMA, the weak IoT device directly detects its desired signal by treating the signal intended to the strong IoT device as interference while the SIC is conducted for decoding signal at the strong IoT device [5]. Therefore, two device would be the preferred model rather than multiple devices in a group result in more interference to devices which make performance degradation.

where $|g_I|^2 \sim \mathcal{CN}(0, \lambda_I)$. For ipSIC, the residual IS, g_I, is modeled as a Rayleigh fading channel with zero mean and variance λ_I for $0 \le \lambda_I < 1$ [33].

Given (4b), U_2 detects the designated signal $\tilde{x}_2$, treating $\tilde{x}_1$ as interference. The instantaneous SINR at U_2 from (4b) gives us

$$\bar{\Gamma}^*_{U_2,\tilde{x}_2} = \frac{\rho_A a_2 \left|h_{n_2^*}\right|^2}{\rho_A a_1 \left|h_{n_2^*}\right|^2 + 1}. \tag{7}$$

B. Channel Characteristics

The probability density function (PDF) of the random variable (RV) $|h_i|^2$ can be derived as follows [22]:

$$f_{|h_i|^2}(x) = \frac{\mu_i^{m_i} x^{m_i-1}}{\Gamma(m_i)} e^{-\mu_i x}, \; i \in \{0, 1, 2\} \tag{8}$$

where $\Gamma(x) = (x-1)!$ is the Gamma function and $\mu_i = (m_i/\lambda_i)$ in which λ_i, and m_i representing the mean and integer fading factor, respectively. According to [34] and [35], we get channel gains of fading as $\lambda_0 = d_{\text{PD}}^{-\alpha}$, $\lambda_1 = d_{U_1}^{-\alpha}$, and $\lambda_2 = d_{U_2}^{-\alpha}$. From [3], we have the cumulative distribution function (CDF) of the instantaneous channel gain $\bar{X}$ as follows:

$$\begin{aligned} F_{|h_i|^2}(x) &= 1 - \frac{\Gamma(m_i, x\mu_i)}{\Gamma(m_i)} \\ &= 1 - e^{-\mu_i x} \sum_{t=0}^{m_i-1} \frac{\mu_i^t x^t}{t!}, \; i \in \{0, 1, 2\} \end{aligned} \tag{9}$$

where $\Gamma(\cdot, \cdot)$ is the upper incomplete Gamma function [36, eq. (8.350.2)].

Therefore, the CDF and PDF of $|h_{n_j^*}|^2$, $j \in \{0, 1, 2\}$ are given as [37, eq. (17)]

$$\begin{aligned} F_{\left|h_{n_j^*}\right|^2}(y) &= \left[1 - \frac{\Gamma(m_j, y\mu_j)}{\Gamma(m_j)}\right]^N \\ &= \sum_{n_j=0}^{N} \sum_{p_j=0}^{n_j(m_j-1)} \binom{N}{n_j} (-1)^{n_j} \mathcal{W}_{p_j}^{n_j,m_j} \mu_j^{p_j} \\ &\quad \times e^{-n_j \mu_j y} y^{p_j} \end{aligned} \tag{10}$$

and

$$\begin{aligned} f_{\left|h_{n_j^*}\right|^2}(y) &= \frac{\partial}{\partial y} F_{\left|h_{n_j^*}\right|^2}(y) \\ &= N \sum_{n_j=0}^{N-1} \sum_{p_j=0}^{n_j(m_j-1)} \binom{N-1}{n_j} (-1)^{n_j} \mathcal{W}_{p_j}^{n_j,m_j} \\ &\quad \times \frac{\mu_j^{p_j+m_j} y^{p_j+m_j-1}}{\Gamma(m_j)} e^{-(n_j+1)\mu_j y} \end{aligned} \tag{11}$$

where $n_j \in \{0, 1, \ldots, N-1\}$, $\binom{n}{k}$ is binomial coefficient $\binom{n}{k} = (n!/k!(n-k)!)$, the intermediate variable $\mathcal{W}_{p_j}^{n_j,m_j}$ $(0 \le p_j \le n_j(m_j-1))$ for positive integers n_j and m_j

denotes the coefficient of the expansion below [38]

$$\left[\sum_{p_j=0}^{m_j-1}\frac{1}{p_j!}\left(x\mu_j\right)^{p_j}\right]^{n_j}=\sum_{p_j=0}^{n_j(m_j-1)}\mathcal{W}_{p_j}^{n_j,m_j}\mu_j^{p_j}x^{p_j} \tag{12}$$

which can be calculated recursively as follows:

$$\mathcal{W}_{p_j}^{n_j,m_j}=\sum_{k=p_j-m_j+1}^{p_j}\frac{\mathcal{W}_k^{n_j-1,m_j}}{\left(p_j-k\right)!}\mathcal{I}_{n_j,m_j}(k) \tag{13}$$

with $\mathcal{W}_0^{n_j,m_j}=1$, $\mathcal{W}_1^{n_j,m_j}=n_j$, $\mathcal{W}_{p_j}^{1,m_j}=1/p_j!$, and

$$\mathcal{I}_{n_j,m_j}(k)=\begin{cases}1, & \text{if } 0\le k\le\left(n_j-1\right)\left(m_j-1\right)\\ 0, & \text{otherwise.}\end{cases} \tag{14}$$

Additionally, Rayleigh-distributed RVs of $|g_I|^2$ have exponential distributions with $f_{|g_I|^2}(x)=(1/\lambda_I)e^{-(x/\lambda_I)}$ and $F_{|g_I|^2}(x)=1-e^{-(x/\lambda_I)}$ [33].

III. Outage Probability Analysis

A. Exact Computation of OP

Since performance of devices in SN and PN are considered in recent work [17], we set higher priority to examine performance of devices at SN. It would be predicted that the devices at the SN have limited performance due to power constraint of the secondary transmitter in (2). As the main performance evaluation, the OP is used since it is the probability of the corresponding SINR falling below a predefined threshold λ, i.e., $P_{\text{out}}=\Pr(Z<\lambda)=F_Z(\lambda)$ [1].

Case 1: From (6a), the OP of the near device with ipSIC case is calculated as follows:

$$\begin{aligned}\mathcal{OP}_1^{\text{ipSIC}}&=\Pr\left(\bar{\Gamma}_{U_1,\bar{x}_2}^{*}<\varepsilon_2\cup\bar{\Gamma}_{U_1,\bar{x}_1}^{*,\text{ipSIC}}<\varepsilon_1\right)\\&=1-\Pr\left(\bar{\Gamma}_{U_1,\bar{x}_2}^{*}\ge\varepsilon_2,\bar{\Gamma}_{U_1,\bar{x}_1}^{*,\text{ipSIC}}\ge\varepsilon_1\right)\end{aligned} \tag{15}$$

where $\Pr(.)$ is the probability operator, $\varepsilon_i=2^{2R_i}-1$, for $i=1,2$ is called as target SINR at U_i.

Replacing $\mathcal{OP}_1^{\text{ipSIC}}$ from (5) and (6a) into (15), we have

$$\begin{aligned}\mathcal{OP}_1^{\text{ipSIC}}&=1-\Pr\left(\hat{Z}_1^{*}\rho_A\ge\phi_2,\hat{Z}_1^{*}\ge\phi_1\left(\rho_A|g_I|^2+1\right)\right)\\&=1-\Pr\left(\hat{Z}_1^{*}\ge\frac{\phi_2}{\rho_A},\hat{Z}_1^{*}>\frac{\phi_1}{\rho_A},|g_I|^2\le\frac{\hat{Z}_1^{*}}{\phi_1}-\frac{1}{\rho_A}\right)\\&=1-\Pr\left(\hat{Z}_1^{*}\ge\frac{\phi_{\max}}{\rho_A},|g_I|^2\le\frac{\hat{Z}_1^{*}}{\phi_1}-\frac{1}{\rho_A}\right)\end{aligned} \tag{16}$$

where $\hat{Z}_1^{*}\triangleq|h_{n_1^{*}}|^2$, $\phi_2=(\varepsilon_2/a_2-\varepsilon_2a_1)$, $\phi_1=(\varepsilon_1/a_1)$ and $\phi_{\max}=\max(\phi_1,\phi_2)$.

It is noted that $\rho_A=\min(\bar{\rho}_A,(\rho_Q/\hat{Z}_0^{*}))$ in which $\hat{Z}_0^{*}\triangleq|h_{n_0^{*}}|^2$, (16) is calculated as follows:

$$\mathcal{OP}_1^{\text{ipSIC}}=1-\mathcal{A}_1-\mathcal{A}_2 \tag{17}$$

where $\mathcal{A}_1\triangleq\Pr(\hat{Z}_1^{*}\ge(\phi_{\max}/\rho_A),|g_I|^2\le(\hat{Z}_1^{*}/\phi_1)-(1/\rho_A),\hat{Z}_0^{*}<(\rho_Q/\bar{\rho}_A))$, $\mathcal{A}_2\triangleq\Pr(\hat{Z}_1^{*}\ge(\phi_{\max}\hat{Z}_0^{*}/\rho_Q),|g_I|^2\le(\hat{Z}_1^{*}/\phi_1)-(\hat{Z}_0^{*}/\rho_Q),\hat{Z}_0^{*}>(\rho_Q/\bar{\rho}_A))$, $\hat{Z}_0^{*}\triangleq|h_{n^{*},0}|^2$, $\bar{\rho}_A=\bar{P}_A/N_0$ denotes the average SNR at the UAV and $\rho_Q=Q/N_0$ denotes the average SNR of interference at the PD.

Proposition 1: The closed-form expression of OP at U_1 with ipSIC is expressed as (18), shown at the bottom of the page, with $\gamma(\cdot,\cdot)$ is the lower incomplete Gamma function [36, eq. (8.350.1)], $\chi_0=(n_0+1)\mu_0-(1/\lambda_I\rho_Q)$, $\chi_1=(n_1+1)\mu_1+(1/\lambda_I\phi_1)$, $\Delta_{\max}=\max((\phi_{\max}/\rho_Q),(\varepsilon_1/a_1\rho_Q))$, $\mathcal{G}(N,n_j,m_j,p_j)=(N/[\Gamma(m_j)])\sum_{n_j=0}^{N-1}\sum_{p_j=0}^{n_j(m_j-1)}\binom{N-1}{n_j}(-1)^{n_j}\mathcal{W}_{p_j}^{n_j,m_j}\mu_j^{p_j+m_j}$ in which $j\in\{0,1,2\}$.

Proof: See Appendix A. ∎

Case 2: From (6b), the OP of U_1 with pSIC is calculated as follows:

$$\begin{aligned}\mathcal{OP}_1^{\text{pSIC}}&=\Pr\left(\bar{\Gamma}_{U_1,\bar{x}_2}^{*}<\varepsilon_2\cup\bar{\Gamma}_{U_1,\bar{x}_1}^{*,\text{pSIC}}<\varepsilon_1\right)\\&=1-\Pr\left(\bar{\Gamma}_{U_1,\bar{x}_2}^{*}\ge\varepsilon_2,\bar{\Gamma}_{U_1,\bar{x}_1}^{*,\text{pSIC}}\ge\varepsilon_1\right)\\&=1-\Pr\left(\hat{Z}_1^{*}\ge\frac{\phi_2}{\rho_A},|g_1|^2\ge\frac{\phi_1}{\rho_A}\right)\\&=1-\Pr\left(\hat{Z}_1^{*}\ge\frac{\phi_{\max}}{\rho_A}\right).\end{aligned} \tag{19}$$

We can easily derive $\mathcal{OP}_1^{\text{pSIC}}$ from (19) as follows:

$$\mathcal{OP}_1^{\text{pSIC}}=1-\mathcal{B}_1-\mathcal{B}_2 \tag{20}$$

where $\mathcal{B}_1=\Pr(\hat{Z}_1^{*}\ge(\phi_{\max}/\bar{\rho}_A),\hat{Z}_0^{*}<(\rho_Q/\bar{\rho}_A))$ and $\mathcal{B}_2=\Pr(\hat{Z}_1^{*}\ge(\phi_{\max}/\rho_Q)\hat{Z}_0^{*},\hat{Z}_0^{*}>(\rho_Q/\bar{\rho}_A))$.

Proposition 2: The closed-form expression of OP at the U_1 with pSIC is determined in (21), shown at the bottom of the next page, with $\varsigma_1=[(n_0+1)\mu_0+\frac{(n_1+1)\mu_1\phi_{\max}}{\rho_Q}]$.

Proof: See Appendix B. ∎

Finally, the OP of $\mathcal{P}_2$ is given by

$$\begin{aligned}\mathcal{OP}_2&=1-\Pr(\bar{\Gamma}_{U_1,\bar{x}_2}^{*}\ge\varepsilon_2)\\&=1-\Pr\left(\hat{Z}_2^{*}\ge\frac{\phi_2}{\bar{\rho}_A},\hat{Z}_0^{*}<\frac{\rho_Q}{\bar{\rho}_A}\right)\\&\quad-\Pr\left(\hat{Z}_2^{*}\ge\frac{\phi_2}{\rho_Q}\hat{Z}_0^{*},\hat{Z}_0^{*}>\frac{\rho_Q}{\bar{\rho}_A}\right)\end{aligned} \tag{22}$$

where $\hat{Z}_2^{*}\triangleq|h_{n_2^{*}}|^2$.

$$\begin{aligned}\mathcal{OP}_1^{\text{ipSIC}}&=1-\mathcal{G}(N,n_0,m_0,p_0)\mathcal{G}(N,n_1,m_1,p_1)\frac{\gamma\left(p_0+m_0,\bar{\rho}_A^{-1}\rho_Q(n_0+1)\mu_0\right)}{[(n_0+1)\mu_0]^{p_0+m_0}}\left\{\frac{\Gamma\left(p_1+m_1,\bar{\rho}_A^{-1}\phi_{\max}(n_1+1)\mu_1\right)}{[(n_1+1)\mu_1]^{p_1+m_1}}-e^{\frac{1}{\bar{\rho}_A\lambda_I}}\frac{\Gamma\left(p_1+m_1,\bar{\rho}_A^{-1}\phi_{\max}\chi_1\right)}{\chi_1^{p_1+m_1}}\right\}\\&\quad-\mathcal{G}(N,n_0,m_0,p_0)\mathcal{G}(N,n_1,m_1,p_1)\left\{\sum_{q=0}^{p_1+m_1-1}\frac{\Gamma(p_1+m_1)\Delta_{\max}{}^{q}\Gamma\left(p_0+q+m_0,\bar{\rho}_A^{-1}\rho_Q[(n_0+1)\mu_0+\Delta_{\max}(n_1+1)\mu_1]\right)}{q![(n_1+1)\mu_1]^{p_1+m_1-q}[(n_0+1)\mu_0+\Delta_{\max}(n_1+1)\mu_1]^{p_0+q+m_0}}-\sum_{q=0}^{p_1+m_1-1}\frac{\Delta_{\max}{}^{q}\Gamma(p_1+m_1)}{q!\chi_1^{p_1+m_1-q}}\right.\\&\quad\left.\times\frac{\Gamma\left(p_0+q+m_0,\bar{\rho}_A^{-1}\rho_Q(\chi_0+\chi_1\Delta_{\max})\right)}{(\chi_0+\chi_1\Delta_{\max})^{p_0+q+m_0}}\right\}\end{aligned} \tag{18}$$

Algorithm 1: Optimization Algorithm to Find a_2^* Based on the Golden Section Search

Input : Initialize $\psi_{\min}=0$, $\psi_{\max}=1$, the golden section search $\varpi=\frac{\sqrt{5}-1}{2}$ and a stopping threshold $\Delta=10^{-3}$
Output: The optimal of a_2^* that minimum the outage performance $\mathcal{OP}_1^{\star}(a_2^*)$, $\star\in\{ipSIC, pSIC\}$

begin
  Create sets $\beta_1=\psi_{\max}-(\psi_{\max}-\psi_{\min})\varpi$ and $\beta_2=\psi_{\min}+(\psi_{\max}-\psi_{\min})\varpi$
  while $|\psi_{\max}-\psi_{\min}|\le\Delta$ **do**
    Update: $\mathcal{OP}_{\text{temp1}}^{\star}=\mathcal{OP}_1^{\star}(\beta_1)$
    Update: $\mathcal{OP}_{\text{temp2}}^{\star}=\mathcal{OP}_1^{\star}(\beta_2)$
    // $\mathcal{OP}_1^{\star}(.)$ is given by (18) and (21)
    if $\mathcal{OP}_{\text{temp1}}^{\star}<\mathcal{OP}_{\text{temp2}}^{\star}$ **then**
      Update: $\psi_{\max}\leftarrow\beta_2$
    else
      Update: $\psi_{\min}\leftarrow\beta_1$
    end
    Update: $\beta_1\leftarrow\psi_{\max}-(\psi_{\max}-\psi_{\min})\varpi$
    Update: $\beta_2\leftarrow\psi_{\min}+(\psi_{\max}-\psi_{\min})\varpi$
  end
  return The optimal of $a_2^*=(\psi_{\max}+\psi_{\min})/2$
end

Similarly, by solving $\mathcal{OP}_1^{\text{pSIC}}$ in (19), $\mathcal{OP}_2$ is obtained in (23), shown at the bottom of the page.

B. Optimal Outage Performance Analysis

Based on the derived OP expressions, it is difficult to obtain closed-form expressions of the optimal values of power allocation factors a_1 and a_2. Fortunately, we can leverage low-complexity algorithms based on the golden section search method to overcome this problem. For example, in Algorithm 1, we present the steps to obtain the exact value of a_2 that minimizes the OP of the first user. The degree of accuracy of Algorithm 1 primarily depends on the given step search Δ.

Although finding optimal OP can be conducted in some cases, the analytical results of OP performance are still complicated, making obtaining any insights difficult. This motivates us to find approximate computation of the main system performance metrics in the next section.

IV. Asymptotic Computation of the Main Performance Metric

Because deriving closed-form expressions do not provide much insight, we analyze the asymptotic expressions for further intuition.

Case 1: For ipSIC, when $\bar{\rho}_A$ goes to infinity then we have $\mathcal{A}_1\approx 0$ and $(\rho_Q/\bar{\rho}_A)\approx 0$, the asymptotic expression for $\mathcal{P}_1^{\infty,\text{ipSIC}}$ is calculated as follows:

$$\begin{aligned}
&\mathcal{OP}_1^{\infty,\text{ipSIC}}\\
&=1-\Pr\left(\hat{Z}_1^*\ge\Delta_{\max}\hat{Z}_0^*,\,|g_I|^2\le\frac{\hat{Z}_1^*}{\phi_1}-\frac{1}{\rho_Q}\hat{Z}_0^*\right)\\
&=1-\int_0^{\infty}f_{\hat{Z}_0^*}(x)\int_{\Delta_{\max}x}^{\infty}f_{\hat{Z}_1^*}(y)\int_0^{\frac{y}{\phi_1}-\frac{x}{\rho_Q}}f_{|g_I|^2}(z)dxdydz\\
&=1-\mathcal{G}(N,n_0,m_0,p_0)\mathcal{G}(N,n_1,m_1,p_1)\\
&\quad\times\int_0^{\infty}x^{p_0+m_0-1}e^{-(n_0+1)\mu_0 x}\int_{\Delta_{\max}x}^{\infty}y^{p_1+m_1-1}e^{-(n_1+1)\mu_1 y}\\
&\quad\times\left(1-e^{-\frac{1}{\lambda_I}\left(\frac{y}{\phi_1}-\frac{x}{\rho_Q}\right)}\right)dxdy.
\end{aligned}\tag{24}$$

Applying [36, eq. (3.361.2)] and [36, eq. (3.361.3)], the integrals in (24) are solved as follows:

$$\begin{aligned}
&\mathcal{OP}_1^{\infty,\text{ipSIC}}\\
&=1-\mathcal{G}(N,n_0,m_0,p_0)\mathcal{G}(N,n_1,m_1,p_1)\\
&\quad\times\left\{\sum_{q=0}^{p_1+m_1-1}\frac{\Delta_{\max}^q\Gamma(p_1+m_1)}{q![(n_1+1)\mu_1]^{p_1+m_1-q}}\right.\\
&\quad\times\frac{\Gamma(p_0+q+m_0)}{[(n_0+1)\mu_0+(n_1+1)\mu_1\Delta_{\max}]^{p_0+q+m_0}}\\
&\quad\left.-\sum_{q=0}^{p_1+m_1-1}\frac{\Delta_{\max}^q\Gamma(p_1+m_1)\Gamma(p_0+q+m_0)}{q!\chi_1^{p_1+m_1-q}[\chi_0+\chi_1\Delta_{\max}]^{p_0+q+m_0}}\right\}.
\end{aligned}\tag{25}$$

Case 2: For pSIC, when $\bar{\rho}_A\to\infty$, $\mathcal{B}_1\approx 0$ and $(\rho_Q/\bar{\rho}_A)\approx 0$, then the asymptotic expression for $\mathcal{OP}_1^{\infty,\text{pSIC}}$ is given by

$$\begin{aligned}
\mathcal{OP}_1^{\infty,pSIC}&=1-\Pr\left(\hat{Z}_1^*\ge\frac{\phi_{\max}}{\rho_Q}\hat{Z}_0^*\right)\\
&=1-\int_0^{\infty}f_{\hat{Z}_0^*}(x)\left[1-F_{\hat{Z}_1^*}\left(\frac{\phi_{\max}}{\rho_Q}x\right)\right]dx
\end{aligned}$$

$$\begin{aligned}
\mathcal{OP}_1^{\text{pSIC}}&=1-\mathcal{G}(N,n_0,m_0,p_0)\mathcal{G}(N,n_1,m_1,p_1)\frac{\gamma\left(p_0+m_0,\bar{\rho}_A^{-1}\rho_Q(n_0+1)\mu_0\right)[(n_1+1)\mu_1]^{p_1-m_1}}{[(n_0+1)\mu_0]^{p_0+m_0}}\Gamma\left(p_1+m_1,(n_1+1)\mu_1\frac{\phi_{\max}}{\bar{\rho}_A}\right)\\
&\quad-\sum_{w=0}^{p_1+m_1-1}\frac{(p_1+m_1-1)!\Gamma\left(p_0+m_0+w,\varsigma_1\rho_Q\bar{\rho}_A^{-1}\right)\phi_{\max}^w}{w![(n_1+1)\mu_1]^{p_1+m_1-w}\varsigma_1^{p_0+m_0+w}\bar{\rho}_Q^w}
\end{aligned}\tag{21}$$

$$\begin{aligned}
\mathcal{OP}_2&=1-\mathcal{G}(N,n_0,m_0,p_0)\mathcal{G}(N,n_2,m_2,p_2)\frac{\gamma\left(p_0+m_0,\bar{\rho}_A^{-1}\rho_Q(n_0+1)\mu_0\right)[(n_2+1)\mu_2]^{p_2-m_2}}{[(n_0+1)\mu_0]^{p_0+m_0}}\Gamma\left(p_2+m_2,(n_2+1)\mu_2\frac{\phi_{\max}}{\bar{\rho}_A}\right)\\
&\quad-\sum_{w=0}^{p_2+m_2-1}\frac{(p_2+m_2-1)!\Gamma\left(p_0+m_0+w,\varsigma_2\rho_Q\bar{\rho}_A^{-1}\right)\phi_{\max}^w}{w![(n_2+1)\mu_2]^{p_2+m_2-w}\varsigma_2^{p_0+m_0+w}\bar{\rho}_Q^w}
\end{aligned}\tag{23}$$

$$= 1 - \mathcal{G}(N, n_0, m_0, p_0) \int_0^\infty x^{p_0+m_0-1} e^{-(n_0+1)\mu_0 x} dx \times \left[1 - \sum_{n_1=0}^{N} \sum_{p_1=0}^{n_1(m_1-1)} \binom{N}{n_1} (-1)^{n_1} \mathcal{W}_{p_1}^{n_1,m_1} \mu_1^{p_1} \rho_Q^{-p_1} \phi_{\max}^{p_1} e^{-\frac{n_1\mu_1\phi_{\max}}{\rho_Q} x} x^{p_1} \right] dx \quad (26)$$

where $\Gamma(n) = (n-1)!$ [36, eq. (8.339.1)].

By using [36, eq. (3.351.3)], (26) is expressed as follows:

$$\mathcal{OP}_1^{\infty,\text{pSIC}} = 1 - \mathcal{G}(N, n_0, m_0, p_0) \left\{ \frac{\Gamma(p_0+m_0)}{[(n_0+1)\mu_0]^{p_0+m_0}} - \sum_{n_1=0}^{N} \sum_{p_1=0}^{n_1(m_1-1)} \binom{N}{n_1} (-1)^{n_1} \mathcal{W}_{p_1}^{n_1,m_1} \mu_1^{p_1} \times \frac{\rho_Q^{p_0+m_0} \phi_{\max}^{p_1} \Gamma(p_0+p_1+m_0)}{\left[(n_0+1)\rho_Q\mu_0 + n_1\mu_1\phi_{\max}\right]^{p_0+p_1+m_0}} \right\}. \quad (27)$$

Similar to $\mathcal{OP}_1^{\infty,\text{pSIC}}$ when $\bar{\rho}_A \to \infty$, we have $\Pr(\hat{Z}_2^* \geq (\phi_2/\bar{\rho}_A), \hat{Z}_0^* < (\rho_Q/\bar{\rho}_A)) \approx 0$ and $(\rho_Q/\bar{\rho}_A) \approx 0$. Therefore, $\mathcal{OP}_2^\infty$ is given by

$$\mathcal{OP}_2^\infty = 1 - \Pr\left(\hat{Z}_2^* \geq \frac{\phi_2}{\rho_Q} \hat{Z}_0^*\right) = 1 - \mathcal{G}(N, n_0, m_0, p_0) \left\{ \frac{\Gamma(p_0+m_0)}{[(n_0+1)\mu_0]^{p_0+m_0}} - \sum_{n_2=0}^{N} \sum_{p_2=0}^{n_2(m_2-1)} \binom{N}{n_2} (-1)^{n_2} \mathcal{W}_{p_2}^{n_2,m_2} \mu_2^{p_2} \right\} \times \frac{\Gamma(p_0+p_1+m_0) \rho_Q^{p_0+m_0} \phi_2^{p_2}}{\left[(n_0+1)\rho_Q\mu_0 + n_2\mu_2\phi_2\right]^{p_0+p_2+m_0}} \Bigg\}. \quad (28)$$

Remark 1: From the definition of the diversity order, which is defined as: $\bar{d} = -\lim_{\bar{\rho}_A \to \infty} ([\log(\mathcal{OP}_i^\infty)]/[\log(\bar{\rho}_A)])$, $i \in \{1, 2\}$, when $\bar{\rho}_A$ goes to infinity, the diversity order of 0 is achieved. We can expect that there exists an error floor at high transmit SNR at the UAV, which is a similar result to [39].

In the following sections, we further examine other system performance metric (EC) to provide a better overall understanding of the considered system for possible applications in practice since similar studies [8], [14] have not addressed this system performance metric. Furthermore, since the closed-form expression for (28) in [10] is difficult to be computed, the Gaussian Chebyshev quadrature is also applied to obtain an approximated (24); while in our paper, we provide a closed-form solution for the OP. The EC is not considered in [10]. To provide a complete evaluation of the system performance metrics, we try to give extra mathematical analysis by considering the EC.

V. Ergodic Capacity Analysis

In this section, the EC performance of each device can be determined for pSIC and ipSIC scenarios. In contrast with [8], we aim to find an approximate expression of EC. Both OP and EC can be verified by using popular software packages, such as Mathematica or MATLAB. In principle, EC is defined as the long-term average achievable data rate obtained without considering any delay constraints.

A. Ergodic Rate of U_1 With Imperfect SIC

In this section, we investigate the EC of the system. The achievable rate of the considered system at U_1 is given as follows [16]:

$$\mathcal{C}_1^{\text{ipSIC}} = \mathbb{E}\left\{\log\left(1 + \bar{\Gamma}_{U_1,\tilde{x}_1}^{*,\text{ipSIC}}\right)\right\}. \quad (29)$$

The ergodic rate of U_1 for ipSIC NOMA can be obtained in the following Proposition 3.

Proposition 3: The closed-form approximate expression of EC for U_1 with ipSIC is given by (30), shown at the bottom of the page, in which $\xi_u = \cos((2u-1/2U)\pi)$, $g(t) = \tan([\pi(t+1)]/4)$, and $\sec^2(x) = 1/\cos^2(x)$.

Proof: See Appendix C. ■

B. Ergodic Rate of U_1 With Perfect SIC

The EC of device U_1 for pSIC case is similar to that of ipSIC one

$$\mathcal{C}_1^{\text{pSIC}} = \mathbb{E}\left\{\log\left(1 + \bar{\Gamma}_{U_1,\tilde{x}_1}^{*,\text{pSIC}}\right)\right\}. \quad (31)$$

Proposition 4: The closed-form approximate expression of EC for U_1 with pSIC is given by (32), shown at the bottom of the next page, in which $\xi_c = \cos((2u-1/2C)\pi)$.

Proof: See Appendix D. ■

C. Ergodic Rate of U_2

The ergodic rate of U_2 for NOMA downlink is given by

$$\mathcal{C}_2 = \mathbb{E}\left\{\log\left(1 + \bar{\Gamma}_{U_1,\tilde{x}_2}^*\right)\right\}. \quad (33)$$

$$\mathcal{C}_1^{\text{ipSIC}} \approx \frac{\pi^2}{8U\ln 2} \sum_{u=1}^{U} \frac{\sqrt{1-\xi_u^2}}{1+g(\xi_u)} \sec^2\left(\frac{\pi}{4}(\xi_u+1)\right) \mathcal{G}(N, n_0, m_0, p_0) \mathcal{G}(N, n_1, m_1, p_1) \left\{ \frac{\gamma\left(p_0+m_0, \rho_Q\bar{\rho}_A^{-1}(n_0+1)\mu_0\right)}{[(n_0+1)\mu_0]^{p_0+m_0}} \sum_{k=0}^{p_1+m_1-1} \sum_{v=0}^{k} \binom{k}{v} \times \frac{v!\Gamma(p_1+m_1)\lambda_I^v a_1^{v-k+1} g(\xi_u)^k e^{-\frac{(n_1+1)\mu_1}{\bar{\rho}_A a_1} g(\xi_u)}}{k![(n_1+1)\mu_1]^{p_1+m_1-k}\left[a_1+g(\xi_u)\lambda_I(n_1+1)\mu_1\right]^{v+1}\bar{\rho}_A^{k-v}} + \sum_{k=0}^{p_1+m_1-1} \sum_{v=0}^{k} \binom{k}{v} \frac{\Gamma(p_1+m_1)(k-v)! a_1^{p_0+m_0+1}}{k!\left[a_1+g(\xi_u)\lambda_I(n_1+1)\mu_1\right]^{k-v+1}} \times \frac{\rho_Q^{p_0+m_0}\lambda_I^{k-v} g(\xi_u)^k \Gamma\left(p_0+m_0+v, \rho_Q\bar{\rho}_A^{-1}\left[(n_0+1)\mu_0 + (\rho_Q a_1)^{-1} g(\xi_u)(n_1+1)\mu_1\right]\right)}{[(n_1+1)\mu_1]^{p_1+m_1-k}\left[\rho_Q a_1(n_0+1)\mu_0 + g(\xi_u)(n_1+1)\mu_1\right]^{p_0+m_0+v}} \right\} \quad (30)$$

By the definition of the expectation operator and after integration-by-part, $\mathcal{C}_2$ can then be evaluated as follows:

$$\mathcal{C}_2 = \frac{1}{2\ln 2}\int_0^{a_2/a_1} \frac{1}{1+x}\bar{F}_{\hat{Z}_2^*}\left(\frac{x}{a_2 - xa_1}\right)dx \tag{34}$$

where $\bar{F}_{\hat{Z}_2^*}(x)$ denotes the complementary CDF of $|h_{n_2^*}|^2$, i.e., $\bar{F}_{\hat{Z}_2^*}(x) = 1 - F_{\hat{Z}_2^*}(x)$. By the variable changing $t = (2a_1x/a_2) - 1$ and after few steps, (34) can then be further derived as follows:

$$\mathcal{C}_2 = \frac{a_2}{4a_1\ln 2}\int_{-1}^{1} \frac{1}{1+\Delta(t)}\bar{F}_{\hat{Z}_2^*}(\Xi(x))dt \tag{35}$$

where $\Delta(t) = (a_2/2a_1)(t+1)$ and $\Xi(t) = ([\Delta(t)]/[a_2 - a_1\Delta(t)])$.

Because $F_{\hat{Z}_2^*}(x)$ in (35) has a similar form to $F_Y(x)$ in (23) and $\mathcal{C}_2$ is given by applying the Gaussian–Chebyshev quadrature we have (36), shown at the bottom of the next page, with $\xi_s = \cos([2s - 1/2S]\pi)$.

Remark 2: With regard to retaining fairness among NOMA devices, the EC of each device is deteriorated by the power allocation factors installed at the UAV since they directly change fairness among two ground devices. It is noted such EC performance mainly depends on the SNR at the UAV along with the power allocation factors a_1 and a_2. We expect to further evaluate such EC performance in the numerical simulation section.

VI. Numerical Results and Discussion

In this section, we numerically evaluate our theoretical results on the OP and EC performance.[8] We set the fading parameters to $m = m_0 = m_1 = m_2$. The Monte Carlo simulation results are averaged over 10^6 independent trials. The target rate has unit of bit per channel user (denoted in short as BPCU). In the following figures, we denote "Ana.," "Sim.," and "Asymp." as analytical computation, Monte Carlo, and asymptotic computation-based simulations, respectively. The other main parameters are summarized in Table II. In addition, the Gauss–Chebyshev parameter is selected as $U = C = S = 100$ to yield a close approximation [40].

[8]In the scope of this article, we do not want to represent transmission block of signal along with the flow chart of such UAV CRNOMA-inspired IoT systems since we can see such results in [17]. We prefer to confirm the validation of our derived theoretical results through the Monte Carlo simulations. The presented numerical results as expected match the simulation results and numerical results, demonstrating the exactness of our work. These performance metrics were also the objective of [8] and [17].

TABLE II
Main Parameters for Our Simulations

Parameters	Notation	Values
Number of antennas (UAV)	N	$1, 3, 5$
Power allocation factors	$\{a_1, a_2\}$	$\{0.2, 0.8\}$
Target rates used to decode $\bar{x}_1$ and $\bar{x}_2$	R_1, R_2	0.5 BPCU
Fading parameter	m	2
Interference constraint at PD	ρ_Q	10 [dB]
Altitude of the UAV	H	45m
Path-loss exponent	α	3.5
Mean values of IS (ipSIC)	λ_I	0.001
Distance between PD and the center point	d_0	20m
Distance between U_1 and the center point	d_1	15m
Distance between U_2 and the center point	d_2	40m

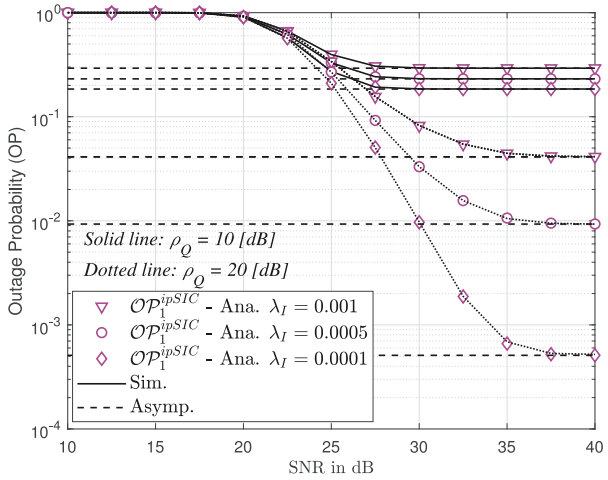

Fig. 2. OP versus the transmit SNR, with the different impact levels of IS at U_1.

In Fig. 2, we show the OP of U_1 with ipSIC against the transmit SNR at the UAV with ($\rho_Q = 20$ [dB] and $\lambda_I = 0.0001$). We observe that U_1 with ipSIC has the best outage performance. Then, the OP of U_1 decreases as λ_I

$$\mathcal{C}_1^{\text{pSIC}} \approx \frac{\pi^2}{8C\ln 2}\sum_{c=1}^{C}\frac{\sqrt{1-\xi_c^2}}{1+g(\xi_c)}\sec^2\left(\frac{\pi}{4}(\xi_c+1)\right)\mathcal{G}(N,n_0,m_0,p_0)\mathcal{G}(N,n_1,m_1,p_1)\left\{\frac{\gamma\left(p_0+m_0,\bar{\rho}_A^{-1}\rho_Q(n_0+1)\mu_0\right)}{[(n_0+1)\mu_0]^{p_0+m_0}}\right.$$
$$\times e^{-\frac{(n_1+1)\mu_1 g(\xi_c)}{\bar{\rho}_A a_1}}\sum_{k=0}^{p_1+m_1-1}\frac{\Gamma(p_1+m_1)g(\xi_c)^k}{k![(n_1+1)\mu_1]^{p_1+m_1-k}\bar{\rho}_A^k a_1^k} + \sum_{k=0}^{p_1+m_1-1}\frac{\Gamma(p_1+m_1)g(\xi_c)^k\rho_Q^{p_0+m_0}a_1^{p_0+m_0}}{k![(n_1+1)\mu_1]^{p_1+m_1-k}}$$
$$\left.\times\frac{\Gamma\left(p_0+m_0+k,\bar{\rho}_A^{-1}\rho_Q\left[(n_0+1)\mu_0+\frac{(n_1+1)\mu_1 g(\xi_c)}{\rho_Q a_1}\right]\right)}{\left[\rho_Q a_1(n_0+1)\mu_0+(n_1+1)\mu_1 g(\xi_c)\right]^{p_0+m_0+k}}\right\} \tag{32}$$

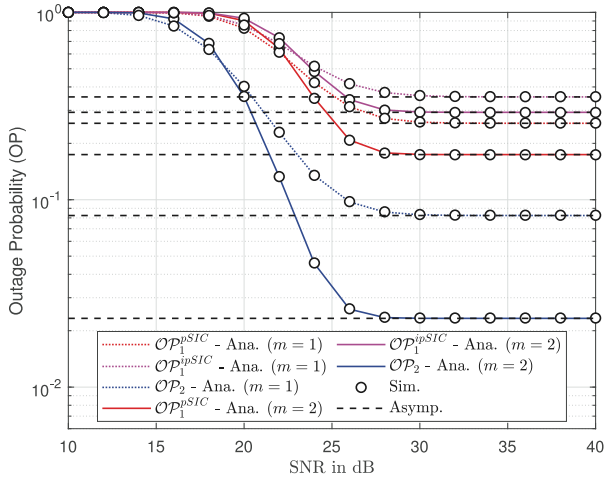

Fig. 3. Comparison of OP with different m fading parameters, with $N = 2$.

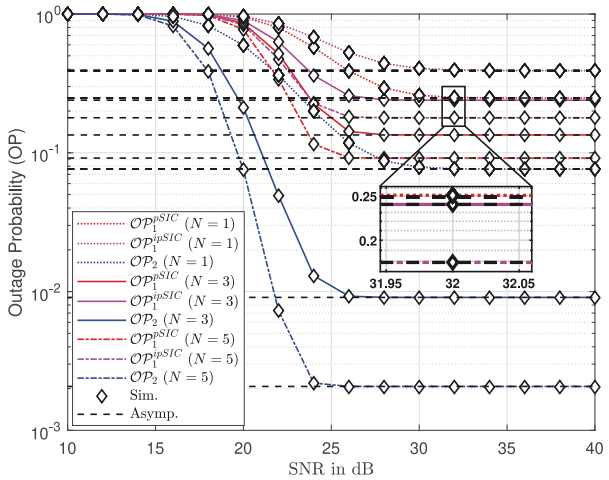

Fig. 4. OP versus the transmit SNRs and the numbers of antennas of the UAV, with $m = 2$.

decreases. This is reasonable since significant ipSIC introduces serious interference to U_1, thereby causing performance degradation for U_1. Similarly, we check that the estimated OP matches the simulation findings. For large $\bar{\rho}_A$ values, the error floor appears, which coincides with our asymptotic analysis in (25).

Fig. 3 shows how the increase in transmit power at the UAV influences the performance of the UAV CRNOMA-inspired IoT system in terms of the OP for a fixed number of antennas at PD, U_1, and U_2. We expect to evaluate the impact of severity of channel on the performance, where $m = 1, 2$ is considered. The lowest OP of each device is obtained with pSIC condition and a fading parameter $m = 2$. It is observed that the OP of the two devices are considerably different at low transmit power, while the outage performance of two devices are similar for a high transmit power. It is also observed that, in general, U_2 has a lower OP compared to U_1. We also verify that the approximate OP matches the simulation results. For large SNR values, the error floor appears, which also matches the asymptotic analysis in (25), (27), and (28), respectively.

Similar observations hold for a different number of antennas as in Fig. 4. The outage performance of the second device decreases as N increases and in our simulations, it reaches its lowest of value for $N = 5$. By comparing a single-antenna UAV to a multiple-antenna one ($N = 3$), we observe that $\mathcal{OP}_1^{\text{pSIC}}$, $\mathcal{OP}_1^{\text{ipSIC}}$, and $\mathcal{OP}_2$ improve by 50%, 40%, and 7%, respectively. If the system increases the number of antennas at a UAV from $N = 3$ to $N = 5$, the improved performance gains of $\mathcal{OP}_1^{\text{pSIC}}$, $\mathcal{OP}_1^{\text{ipSIC}}$, and $\mathcal{OP}_2$ are 30.7%, 25.4%, and 77.7%, respectively. It is worth noting that the first device (U_1) associated with the ipSIC case degrades significantly for the three considered cases of the number of antennas.

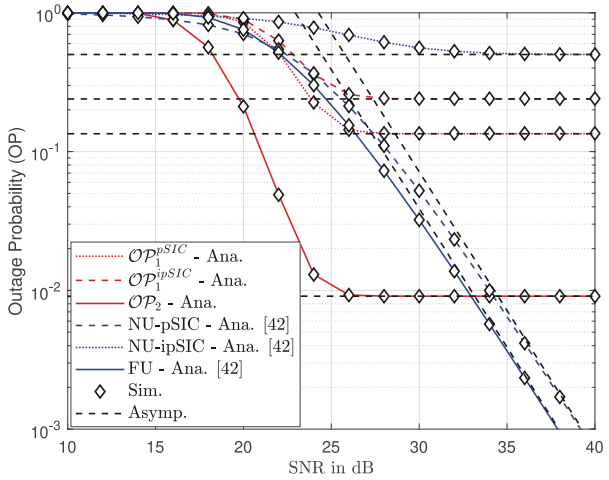

Fig. 5. Comparison between our work and the recent work [41], with $N = 3$, $H = 45$ m, $\gamma_{thn} = \varepsilon_1 = \gamma_{thf} = \varepsilon_2 = 1$, and other parameters are taken from [41].

Fig. 5 compares the OP of the near user (NU) in pSIC and ipSIC cases, the far user (FU), and two users in our system versus SNR. At low SNR values (SNR is less than 25 dB), the OPs of the two users in our system exhibits better performance in comparison to the OPs in [41]. However, a fair comparison

$$\mathcal{C}_2 \approx \frac{\pi a_2}{4Sa_1 \ln 2} \sum_{s=1}^{S} \frac{\sqrt{1-\xi_s^2}}{1+\Delta(\xi_s)} \mathcal{G}(N, n_0, m_0, p_0)\mathcal{G}(N, n_2, m_2, p_2) \left\{ \frac{\gamma\left(p_0+m_0, \bar{\rho}_A^{-1}\rho_Q(n_0+1)\mu_0\right)}{[(n_0+1)\mu_0]^{p_0+m_0}} e^{-\frac{(n_2+1)\mu_2\Xi(\xi_s)}{\bar{\rho}_A}} \right.$$
$$\times \sum_{k=0}^{p_2+m_2-1} \frac{\Gamma(p_2+m_2)\Xi(\xi_s)^k}{k![(n_2+1)\mu_2]^{p_2+m_2-k}\bar{\rho}_A^k} + \sum_{k=0}^{p_2+m_2-1} \frac{\Gamma(p_2+m_2)\Xi(\xi_s)^k \rho_Q^{p_0+m_0}}{k![(n_2+1)\mu_2]^{p_2+m_2-k}\left[\rho_Q(n_0+1)\mu_0+(n_2+1)\mu_2\Xi(\xi_s)\right]^{p_0+m_0+k}}$$
$$\left. \times \Gamma\left(p_0+m_0+k, \bar{\rho}_A^{-1}\rho_Q\left[(n_0+1)\mu_0+\frac{(n_2+1)\mu_2\Xi(\xi_s)}{\rho_Q}\right]\right)\right\} \tag{36}$$

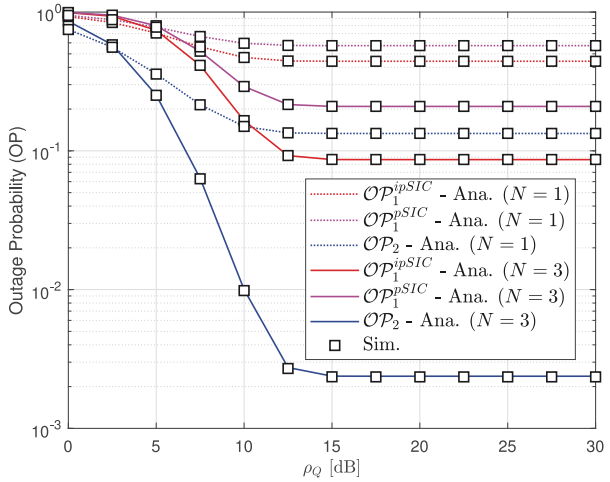

Fig. 6. OP versus the maximum available transmit power of secondary source, with $\bar{\rho}_A = 25$ [dB].

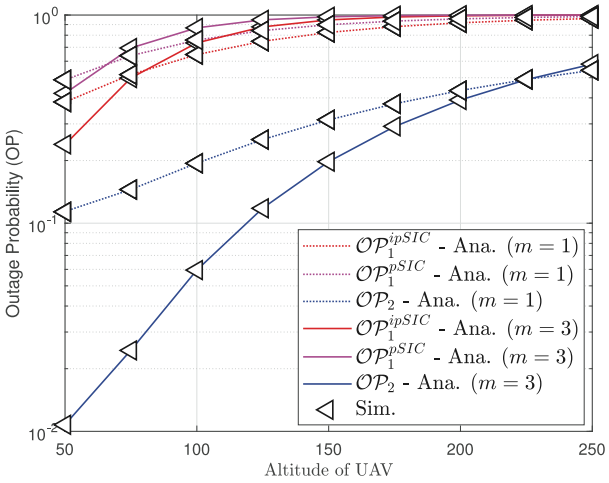

Fig. 8. OP performance with different UAV altitude, with $N = 2$ and $\bar{\rho}_A = 25$ [dB].

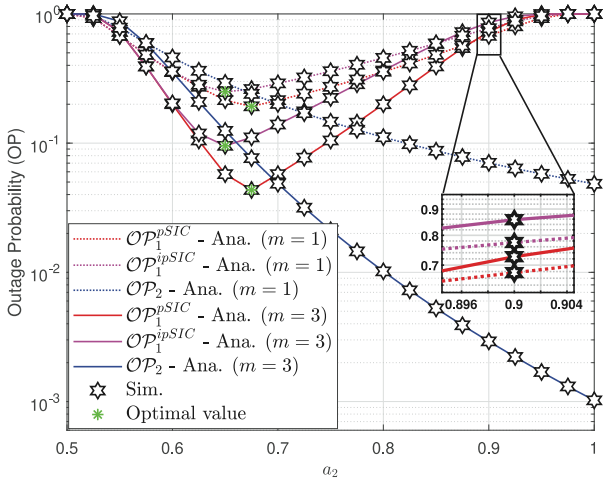

Fig. 7. OP versus the power allocation factors, with $\bar{\rho}_A = 25$ dB.

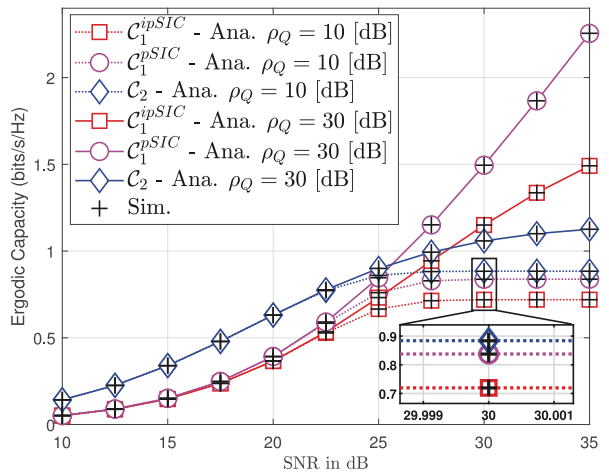

Fig. 9. EC versus transmit SNR at UAV, with $N = 4$, $m = 2$, and $\lambda_I = 0.001$.

is hard to realize, the SN deals with sharing spectrum to work together with the PN and the users in the SN are affected by the transmit power limitations (2). One can observe that an outage floor exists in the high SNR regime due to such power constraint, which makes OP performance in our system (for the case of the second user) worse than work in [41] when SNR is greater than 33 dB.

The OP of the UAV CRNOMA-inspired IoT system is shown against ρ_Q in Fig. 6. The OP is dependent on the interference power, which affects the transmit SNR of the secondary source, as illustrated in this diagram. As a result, the OP patterns are comparable to those seen in Fig. 4. Further, the intuitive results of saturated curves of OP reported in Figs. 3–6 confirm diversity order "0" as Remark 1 mentioned. It can be explained that such OP cannot be improved more at high SNR as it depends on other parameters.

In Fig. 7, the ideal OP of U_1 with ipSIC and U_1 with pSIC are illustrated as well as the impact of the power-splitting factor a_2. For U_1 with ipSIC, the lowest point of the OP occurs at $a_2 = 0.65$, which also coincides with the result given by Algorithm 1. On the other hand, U_2's outage performance improves if a_2 increases from 0 to 0.5. This can be explained by the fact that utilizing SINR to identify signal $\bar{x}_2$ in (7) is dependent on a_2, and that SINR in turn affects the OP. As a result, changing the value of a_2 can influence the performance difference between these nodes.

In Fig. 8, we look at the OP for various UAV heights with a transmit SNR of 25 [dB]. The curves of pSIC and ipSIC cases are overlapped with each other for the fading parameter m as seen in this diagram. As shown in Fig. 8, the OP rises as the height of the UAV grows, implying that when the distance between the UAV and ground device is too great, the UAV will be unable to connect with ground devices with the provided transmit power. This is due to the fact that path loss rises as the distance between the UAV and the device grows, resulting in an increase in OP.

Fig. 9 shows that the EC of these nodes may be increased in the high SNR regime, ρ_A, resulting in more reliable transmission. Fig. 9 depicts the EC performance. U_1 has the best EC of the two nodes. The EC of the considered system increases considerably when ρ_A is increased from 10 to 35 [dB]. When ρ_A is larger than 30 [dB], the EC encounters an upper constraint analogous to the situation for the OP.

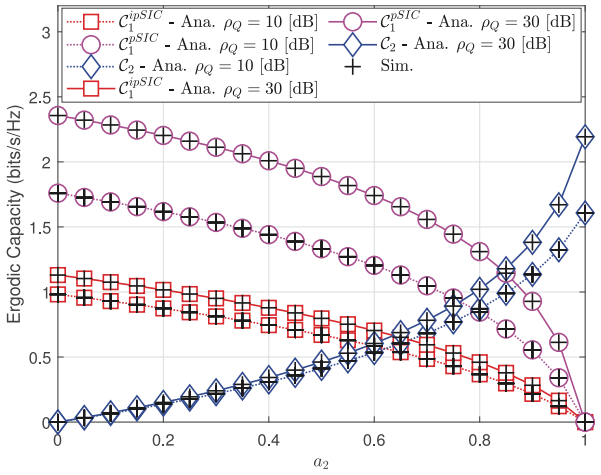

Fig. 10. EC versus a_2 for $N = 4$, $m = 2$, and $\lambda_I = 0.001$.

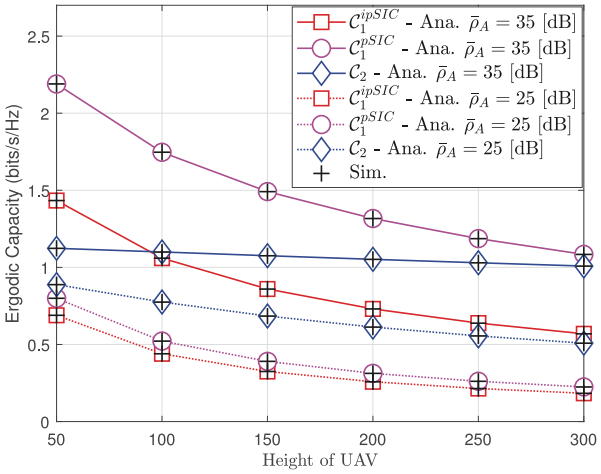

Fig. 11. EC performance with an ideal target rate for different UAV altitudes, with $N = 4$, $m = 2$, and $\rho_Q = 30$ [dB].

The EC versus a_2 is examined for various values of the temperature-constraint-to-noise ratio ρ_Q (i.e., $\rho_Q = 10, 30$ [dB]) in Fig. 10. The EC values of the two devices move in opposite directions. It indicates that while U_1's EC grows, U_2's decreases in the a_2 range of 0 to 1. The EC diminishes as ρ_Q decreases. This can be explained by the fact that EC is proportional to the temperature-constraint-to-noise ratio ρ_Q; the higher the ρ_Q, the better the transmission's quality.

As seen from Fig. 11, the ergodic rates of the system decrease as the altitude of the UAV increases for fixed fading parameter m and transmit power. As the UAV altitude increases, it shows the loss of connection between the UAV and the ground device affects the performance of the system. The simulation here includes the curves for both perfect and imperfect SIC, and as expected, the former performs better.

Finally, to further analyze how the antenna selection scheme benefits to such system, we evaluate the EC with respect to varying N in Fig. 12. The other parameters are set as follows: $m = 2$, $\lambda_I = 0.01$, and $\rho_Q = 30$ [dB]. The EC will improve once the system includes a higher number of transmit antennas N at the UAV. An important observation is that the EC of

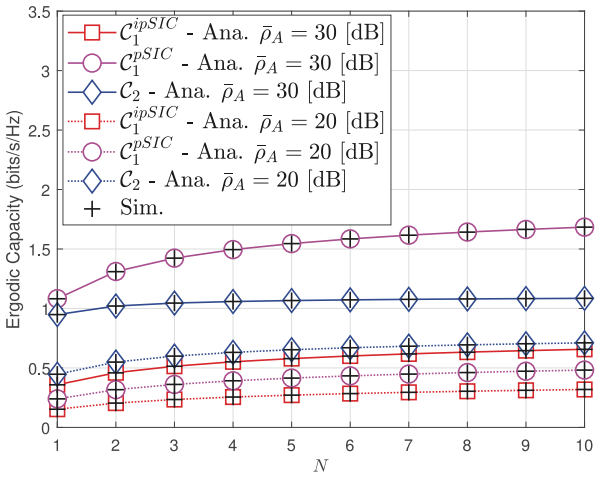

Fig. 12. EC with increasing number of antennas at the UAV, N, for $m = 2$, $\lambda_I = 0.010$, and $\rho_Q = 30$ [dB].

device U_1 is more sensitive with affection by varying N than another. It is interesting to us when the UAV equipped a small number of transmit antennas, i.e., $N = 5$ is enough to archive EC improvement as expected. More importantly, we can conclude from these experimental results that such IoT system experiences not only low cost but also improved performance of OP and EC.

VII. Conclusion

In this article, we have considered an UAV CRNOMA-inspired IoT system in the presence of a multiantenna UAV assisting the devices of the SN over channels with Nakagami-m fading. We analyzed the performance of the system with perfect and imperfect SIC in various aspects, such as power allocation factors, the altitude of the UAV, the number of antennas at the UAV, and the transmit SNR at the UAV. To characterize the main system performance metrics, the performance of the UAV CRNOMA-inspired IoT system was analyzed thoroughly in terms of the OP and the EC. We also provided an algorithm to find the optimal outage behavior for the ground IoT users. The analysis shows that power allocation factors, the number of antennas, and the altitude of the UAV play a major role in the outage performance improvement for both pSIC and ipSIC scenarios. As power allocation increases, at higher average SNR levels from the UAV, the system has a better EC performance compared to other cases. As the distance between the UAV and the ground devices increases, the performance of the device decreases due to loss of signal quality; whereas increasing the number of antennas at the UAV has enhances the performance in such cases. In future work, we will integrate UAV CRNOMA with reconfigurable intelligent surfaces to further improve system performance metrics.

Appendix A
Proof of Proposition 1

From (17), with the help of (11) and PDF of $|g_I|^2$, $\mathcal{A}_1$ can be further computed by

$$\mathcal{A}_1 = \Pr\left(\hat{Z}_1^* \geq \frac{\phi_{\max}}{\rho_A}, |g_I|^2 \leq \frac{\hat{Z}_1^*}{\phi_1} - \frac{1}{\rho_A}, \hat{Z}_0^* < \frac{\rho_Q}{\bar{\rho}_A}\right)$$
$$= \int_0^{\frac{\rho_Q}{\bar{\rho}_A}} f_{\hat{Z}_0^*}(x) \int_{\frac{\phi_{\max}}{\rho_A}}^{\infty} f_{\hat{Z}_1^*}(y) \int_0^{\frac{y}{\phi_1}-\frac{1}{\bar{\rho}_A}} f_{|g_I|^2}(z) dxdydz$$
$$= \frac{\mathcal{G}(N, n_0, m_0, p_0)\mathcal{G}(N, n_1, m_1, p_1)}{\lambda_I} \times \int_0^{\frac{\rho_Q}{\bar{\rho}_A}} x^{p_0+m_0-1} e^{-(n_0+1)\mu_0 x} \int_{\frac{\phi_{\max}}{\rho_A}}^{\infty} y^{p_1+m_1-1} e^{-(n_1+1)\mu_1 y} \times \int_0^{\frac{y}{\phi_1}-\frac{1}{\bar{\rho}_A}} e^{-\frac{z}{\lambda_I}} dxdydz \quad (37)$$

where

$$\mathcal{G}(N, n_j, m_j, p_j) = \frac{N}{\Gamma(m_j)} \sum_{n_j=0}^{N-1} \sum_{p_j=0}^{n_j(m_j-1)} \binom{N-1}{n_j} \times (-1)^{n_j} \mathcal{W}_{p_j}^{n_j, m_j} \mu_j^{p_j+m_j}. \quad (38)$$

Next, $\mathcal{A}_1$ can be obtained by using [36, eq. (3.351.1)] and it is equivalent to

$$\mathcal{A}_1 = \mathcal{G}(N, n_0, m_0, p_0)\mathcal{G}(N, n_1, m_1, p_1) \times \frac{\gamma\left(p_0+m_0, \bar{\rho}_A^{-1}\rho_Q(n_0+1)\mu_0\right)}{[(n_0+1)\mu_0]^{p_0+m_0}} \times \left(\mathcal{A}_{1,1} - \mathcal{A}_{1,2}\right) \quad (39)$$

where $\mathcal{A}_{1,1} = \int_{(\phi_{\max}/\bar{\rho}_A)}^{\infty} y^{p_1+m_1-1} e^{-(n_1+1)\mu_1 y} dy$, $\mathcal{A}_{1,2} = e^{(1/\bar{\rho}_A\lambda_I)} \int_{(\phi_{\max}/\bar{\rho}_A)}^{\infty} y^{p_1+m_1-1} e^{-\chi_1 y} dy$ and $\chi_1 = (n_1+1)\mu_1 + (1/\lambda_I\phi_1)$.

Based on (39), by applying [36, eq. (3.351.2)] and with some further manipulations we can obtain the final expression of $\mathcal{A}_{1,1}$ and $\mathcal{A}_{1,2}$ are given by

$$\mathcal{A}_{1,1} = \frac{\Gamma\left(p_1+m_1, \bar{\rho}_A^{-1}\phi_{\max}(n_1+1)\mu_1\right)}{[(n_1+1)\mu_1]^{p_1+m_1}} \quad (40a)$$

$$\mathcal{A}_{1,2} = e^{\frac{1}{\bar{\rho}_A\lambda_I}} \frac{\Gamma\left(p_1+m_1, \bar{\rho}_A^{-1}\phi_{\max}\chi_1\right)}{\chi_1^{p_1+m_1}}. \quad (40b)$$

Putting (40b) and (40a) into (39), we have new expression of $\mathcal{A}_1$ as follows:

$$\mathcal{A}_1 = \mathcal{G}(N, n_0, m_0, p_0)\mathcal{G}(N, n_1, m_1, p_1) \times \frac{\gamma\left(p_0+m_0, \bar{\rho}_A^{-1}\rho_Q(n_0+1)\mu_0\right)}{[(n_0+1)\mu_0]^{p_0+m_0}} \times \left\{ \frac{\Gamma\left(p_1+m_1, \bar{\rho}_A^{-1}\phi_{\max}(n_1+1)\mu_1\right)}{[(n_1+1)\mu_1]^{p_1+m_1}} - e^{\frac{1}{\bar{\rho}_A\lambda_I}} \frac{\Gamma\left(p_1+m_1, \bar{\rho}_A^{-1}\phi_{\max}\chi_1\right)}{\chi_1^{p_1+m_1}} \right\}. \quad (41)$$

After some algebraic manipulations, $\mathcal{A}_2$ is calculated as follows:

$$\mathcal{A}_2 = \Pr\left(\hat{Z}_1^* \geq \frac{\phi_{\max}\hat{Z}_0^*}{\rho_Q}, |g_I|^2 \leq \frac{\hat{Z}_1^*}{\phi_1} - \frac{\hat{Z}_0^*}{\rho_Q}, \hat{Z}_0^* > \frac{\rho_Q}{\bar{\rho}_A}\right)$$
$$= \Pr\left(\begin{matrix}\hat{Z}_1^* \geq \frac{\phi_{\max}\hat{Z}_0^*}{\rho_Q}, |g_I|^2 \leq \frac{\hat{Z}_1^*}{\phi_1} - \frac{\hat{Z}_0^*}{\rho_Q}, \hat{Z}_0^* > \frac{\rho_Q}{\bar{\rho}_A}, \\ \hat{Z}_1^* > \frac{\phi_1\hat{Z}_0^*}{\rho_Q}\end{matrix}\right)$$
$$= \Pr\left(\hat{Z}_1^* \geq \Delta_{\max}\hat{Z}_0^*, |g_I|^2 \leq \frac{\hat{Z}_1^*}{\phi_1} - \frac{\hat{Z}_0^*}{\rho_Q}, \hat{Z}_0^* > \frac{\rho_Q}{\bar{\rho}_A}\right)$$
$$= \int_{\frac{\rho_Q}{\bar{\rho}_A}}^{\infty} f_{\hat{Z}_0^*}(x) \int_{\Delta_{\max}x}^{\infty} f_{\hat{Z}_1^*}(y) \int_0^{\frac{y}{\phi_1}-\frac{x}{\rho_Q}} f_{|g_I|^2}(z) dxdydz$$
$$= \int_{\frac{\rho_Q}{\bar{\rho}_A}}^{\infty} f_{\hat{Z}_0^*}(x) \int_{\Delta_{\max}x}^{\infty} f_{\hat{Z}_1^*}(y) \left[1 - e^{-\frac{1}{\lambda_I}\left(\frac{y}{\phi_1}-\frac{x}{\rho_Q}\right)}\right] dxdy$$
$$= \mathcal{G}(N, n_0, m_0, p_0)\mathcal{G}(N, n_1, m_1, p_1)\left[\mathcal{A}_{2,1} - \mathcal{A}_{2,2}\right] \quad (42)$$

where $\Delta_{\max} = \max([\phi_{\max}\hat{Z}_0^*]/\rho_Q, [\phi_1/\rho_Q])$, $\chi_0 = (n_0+1)\mu_0 - (1/\lambda_I\rho_Q)$, and

$$\mathcal{A}_{2,1} = \int_{\frac{\rho_Q}{\bar{\rho}_A}}^{\infty} x^{p_0+m_0-1} e^{-(n_0+1)\mu_0 x} \times \int_{\Delta_{\max}x}^{\infty} y^{p_1+m_1-1} e^{-(n_1+1)\mu_1 y} dxdy \quad (43a)$$

$$\mathcal{A}_{2,2} = \int_{\frac{\rho_Q}{\bar{\rho}_A}}^{\infty} x^{p_0+m_0-1} e^{-\chi_0 x} \int_{\Delta_{\max}x}^{\infty} y^{p_1+m_1-1} e^{-\chi_1 y} dxdy. \quad (43b)$$

With the help [36, eq. (3.351.2)] and after some algebraic manipulations, $\mathcal{A}_{2,1}$ and $\mathcal{A}_{2,2}$ are given by

$$\mathcal{A}_{2,1} = \sum_{q=0}^{p_1+m_1-1} \frac{\Gamma(p_1+m_1)\Delta_{\max}^q}{q![(n_1+1)\mu_1]^{p_1+m_1-q}} \times \int_{\frac{\rho_Q}{\bar{\rho}_A}}^{\infty} x^{p_0+q+m_0-1} e^{-[(n_0+1)\mu_0+\Delta_{\max}(n_1+1)\mu_1]x} dx$$
$$= \sum_{q=0}^{p_1+m_1-1} \frac{\Gamma(p_1+m_1)\Delta_{\max}^q}{q![(n_1+1)\mu_1]^{p_1+m_1-q}} \times \frac{\Gamma\left(p_0+q+m_0, \bar{\rho}_A^{-1}\rho_Q[(n_0+1)\mu_0+\Delta_{\max}(n_1+1)\mu_1]\right)}{[(n_0+1)\mu_0+\Delta_{\max}(n_1+1)\mu_1]^{p_0+q+m_0}} \quad (44)$$

and

$$\mathcal{A}_{2,2} = \sum_{q=0}^{p_1+m_1-1} \frac{\Gamma(p_1+m_1)\Delta_{\max}^q}{q!\chi_1^{p_1+m_1-q}} \times \int_{\frac{\rho_Q}{\bar{\rho}_A}}^{\infty} x^{p_0+q+m_0-1} e^{-(\chi_0+\chi_1\Delta_{\max})x} dx$$
$$= \sum_{q=0}^{p_1+m_1-1} \frac{\Delta_{\max}^q\Gamma(p_1+m_1)}{q!\chi_1^{p_1+m_1-q}(\chi_0+\chi_1\Delta_{\max})^{p_0+q+m_0}} \times \Gamma\left(p_0+q+m_0, \bar{\rho}_A^{-1}\rho_Q(\chi_0+\chi_1\Delta_{\max})\right) \quad (45)$$

where $\Delta_{\max} = \max((\phi_{\max}/\rho_Q), (\varepsilon_1/a_1\rho_Q))$ and $\chi_0 = (n_0+1)\mu_0 - (1/\lambda_I\rho_Q)$.

Substituting (37) into (38), $\mathcal{A}_2$ is written as (46), shown at the bottom of the next page.

Combining (46) and (41), we can obtain (18).

The proof of Proposition 1 is completed.

APPENDIX B
PROOF OF PROPOSITION 1

It can be recalled $\mathcal{B}_1$ in (20) as follows:

$$\begin{aligned}\mathcal{B}_1 &= \Pr\left(\hat{Z}_1^* \geq \frac{\phi_{\max}}{\bar{\rho}_A}, \hat{Z}_0^* < \frac{\rho_Q}{\bar{\rho}_A}\right)\\ &= \int_0^{\frac{\rho_Q}{\bar{\rho}_A}} f_{\hat{Z}_0^*}(x) \int_{\frac{\phi_{\max}}{\bar{\rho}_A}}^{\infty} f_{\hat{Z}_1^*}(y) dxdy\\ &= \mathcal{G}(N, n_0, m_0, p_0)\mathcal{G}(N, n_1, m_1, p_1)\\ &\quad \times \int_0^{\frac{\rho_Q}{\bar{\rho}_A}} x^{p_0+m_0-1} e^{-(n_0+1)\mu_0 x} \int_{\frac{\phi_{\max}}{\bar{\rho}_A}}^{\infty} y^{p_1+m_1-1} e^{-(n_1+1)\mu_1 y}\\ &\quad \times dxdy. \end{aligned} \tag{47}$$

Applying [36, eq. (3.351.1)] and [36, eq. (3.351.2)], $\mathcal{B}_1$ is now calculated as follows:

$$\begin{aligned}\mathcal{B}_1 &= \mathcal{G}(N, n_0, m_0, p_0)\mathcal{G}(N, n_1, m_1, p_1)\\ &\quad \times \frac{\gamma\left(p_0+m_0, \bar{\rho}_A^{-1}\rho_Q(n_0+1)\mu_0\right)[(n_1+1)\mu_1]^{p_1-m_1}}{[(n_0+1)\mu_0]^{p_0+m_0}}\\ &\quad \times \Gamma\left(p_1+m_1, (n_1+1)\mu_1\frac{\phi_{\max}}{\bar{\rho}_A}\right). \end{aligned} \tag{48}$$

Similar to (48), after some algebraic manipulations and using [36, eq. (3.351.2)], $\mathcal{B}_2$ is given by

$$\begin{aligned}\mathcal{B}_2 &= \Pr\left(\hat{Z}_1^* \geq \frac{\phi_{\max}}{\rho_Q}\hat{Z}_0^*, \hat{Z}_0^* > \frac{\rho_Q}{\bar{\rho}_A}\right)\\ &= \int_{\frac{\rho_Q}{\bar{\rho}_A}}^{\infty} f_{\hat{Z}_0^*}(x) \int_{\frac{\phi_{\max}}{\rho_Q}x}^{\infty} f_{\hat{Z}_1^*}(y) dxdy\\ &= \mathcal{G}(N, n_0, m_0, p_0)\mathcal{G}(N, n_1, m_1, p_1)\\ &\quad \times \int_{\frac{\rho_Q}{\bar{\rho}_A}}^{\infty} x^{p_0+m_0-1} e^{-(n_0+1)\mu_0 x} \int_{\frac{\phi_{\max}}{\rho_Q}x}^{\infty} y^{p_1+m_1-1} e^{-(n_1+1)\mu_1 y}\\ &\quad \times dxdy\\ &= \mathcal{G}(N, n_0, m_0, p_0)\mathcal{G}(N, n_1, m_1, p_1)\\ &\quad \times \sum_{w=0}^{p_1+m_1-1} \frac{(p_1+m_1-1)!\phi_{\max}^w}{w![(n_1+1)\mu_1]^{p_1+m_1-w}\rho_Q^w}\\ &\quad \times \int_{\frac{\rho_Q}{\bar{\rho}_A}}^{\infty} x^{p_0+m_0+w-1} e^{-\varsigma x} dxdy\\ &= \sum_{w=0}^{p_1+m_1-1} \frac{(p_1+m_1-1)!\phi_{\max}^w}{w![(n_1+1)\mu_1]^{p_1+m_1-w}\bar{\rho}_Q^w}\\ &\quad \times \frac{\Gamma\left(p_0+m_0+w, \varsigma\rho_Q\bar{\rho}_A^{-1}\right)}{\varsigma^{p_0+m_0+w}} \end{aligned} \tag{49}$$

where $\varsigma_a = [(n_0+1)\mu_0 + ([(n_a+1)\mu_a\phi_{\max}]/\rho_Q)]$ in which $a \in \{1, 2\}$.

Substituting (49) and (48) into (19), the OP at U_1 with pSIC regime can be obtained in (21), as shown at the bottom of the p. 6.

The proof of Proposition 2 is completed.

APPENDIX C
PROOF OF PROPOSITION 2

The expression of considered EC $\mathcal{C}_1^{\text{ipSIC}}$ with ipSIC is formulated by

$$\begin{aligned}\mathcal{C}_1^{\text{ipSIC}} &= \mathbb{E}\left\{\log\left(1 + \frac{\rho_A a_1 \hat{Z}_1^*}{\underbrace{\rho_A|g_I|^2+1}_{X}}\right)\right\}\\ &= \frac{1}{2\ln 2}\int_0^{\infty} \frac{1-F_X(x)}{1+x}dx. \end{aligned} \tag{50}$$

Hence, $F_X(x)$ is calculated by

$$F_X(x) = 1 - [\mathcal{V}_1 + \mathcal{V}_2] \tag{51}$$

where $\mathcal{V}_1 = \Pr(\hat{Z}_1^* > x((|g_I|^2/a_1) + (1/\bar{\rho}_A a_1)), \hat{Z}_0^* < (\rho_Q/\bar{\rho}_A))$ and $\mathcal{V}_2 = \Pr(\hat{Z}_1^* > x((|g_I|^2/a_1) + (\hat{Z}_0^*/\rho_Q a_1)), \hat{Z}_0^* > (\rho_Q/\bar{\rho}_A))$.

With the help of [36, eqs. (3.351.1) and (3.351.2)] and after some manipulations we have $\mathcal{V}_1$ and $\mathcal{V}_2$ shown in (52), at the bottom of the next page.

Using Newton's binomial, i.e., $(a+x)^k = \sum_{v=0}^{k}\binom{k}{v}x^v a^{k-v}$ and [36, eqs. (3.351.2) and (3.351.3)], we obtain the closed-form expression of $\mathcal{V}_1$ and $\mathcal{V}_2$.

Substituting (53b) and (53a), shown at the bottom of the next page, into (50), and exchanging the variable $t = (4/\pi)\arctan(x) - 1$, then we have $\tan([\pi(t+1)]/4) = x$, $(\pi/4)\sec^2([\pi/4](t+1))dt = dx$. Finally, $\mathcal{C}_1^{\text{ipSIC}}$ is given by (54), shown at the top of p. 8028, where $g(t) = \tan(\pi(t+1)/4)$ and $\sec^2(x) = 1/\cos^2(x)$.

Unfortunately, finding a closed-form expression for $\mathcal{C}_1^{\text{ipSIC}}$ is tough task, but an accurate approximation can be obtained for it. By using the Gaussian–Chebyshev quadrature [42, eq. (25.4.38)], it is achieved in (55), shown at the top of p. 8028, in which $\xi_u = \cos([2u-1/2U]\pi)$.

The proof is completed.

APPENDIX D
PROOF OF PROPOSITION 4

By invoking (31), $\mathcal{C}_1^{\text{pSIC}}$ is written by

$$\begin{aligned}\mathcal{C}_1^{\text{pSIC}} &= \mathbb{E}\left\{\log\left(1 + \underbrace{\rho_A a_1 \hat{Z}_1^*}_{Y}\right)\right\}\\ &= \frac{1}{2\ln 2}\int_0^{\infty} \frac{1-F_Y(x)}{1+x}dx. \end{aligned} \tag{56}$$

$$\begin{aligned}\mathcal{A}_2 = \mathcal{G}(N, n_0, m_0, p_0)\mathcal{G}(N, n_1, m_1, p_1)\Bigg\{&\sum_{q=0}^{p_1+m_1-1} \frac{\Gamma(p_1+m_1)\Delta_{\max}^q \Gamma\left(p_0+q+m_0, \bar{\rho}_A^{-1}\rho_Q[(n_0+1)\mu_0 + \Delta_{\max}(n_1+1)\mu_1]\right)}{q![(n_1+1)\mu_1]^{p_1+m_1-q}[(n_0+1)\mu_0 + \Delta_{\max}(n_1+1)\mu_1]^{p_0+q+m_0}}\\ &- \sum_{q=0}^{p_1+m_1-1} \frac{\Delta_{\max}^q \Gamma(p_1+m_1)\Gamma\left(p_0+q+m_0, \bar{\rho}_A^{-1}\rho_Q(\chi_0+\chi_1\Delta_{\max})\right)}{q!\chi_1^{p_1+m_1-q}(\chi_0+\chi_1\Delta_{\max})^{p_0+q+m_0}}\Bigg\} \end{aligned} \tag{46}$$

We then have $F_Y(x)$ which is calculated by

$$\begin{aligned} F_Y(x) &= 1 - \Pr\left(\rho_A a_1 \hat{Z}_1^* > x\right) \\ &= 1 - \left[\Pr\left(\hat{Z}_1^* > \frac{x}{\bar{\rho}_A a_1}, \hat{Z}_0^* < \frac{\rho_Q}{\bar{\rho}_A}\right) \right. \\ &\quad \left. + \Pr\left(\hat{Z}_1^* > \frac{x\hat{Z}_0^*}{\rho_Q a_1}, \hat{Z}_0^* > \frac{\rho_Q}{\bar{\rho}_A}\right)\right] \\ &= 1 - \left[\int_0^{\frac{\rho_Q}{\bar{\rho}_A}} f_{\hat{Z}_0^*}(y) \int_{\frac{x}{\bar{\rho}_A a_1}}^{\infty} f_{\hat{Z}_1^*}(z)\, dydz \right. \\ &\quad \left. + \int_{\frac{\rho_Q}{\bar{\rho}_A}}^{\infty} f_{\hat{Z}_0^*}(y) \int_{\frac{xy}{\rho_Q a_1}}^{\infty} f_{\hat{Z}_1^*}(z) dydz\right] \end{aligned} \tag{57}$$

The $F_Y(x)$ in (57) can be acquired via the help of [36, eqs. (3.351.1) and (3.351.2)] as follows:

$$\begin{aligned} F_Y(x) &= 1 - \mathcal{G}(N, n_0, m_0, p_0)\mathcal{G}(N, n_1, m_1, p_1) \\ &\quad \times \left\{ \frac{\gamma\left(p_0 + m_0, \bar{\rho}_A^{-1}\rho_Q(n_0+1)\mu_0\right)}{[(n_0+1)\mu_0]^{p_0+m_0}} \right. \\ &\quad \times e^{-\frac{(n_1+1)\mu_1 x}{\bar{\rho}_A a_1}} \sum_{k=0}^{p_1+m_1-1} \frac{\Gamma(p_1+m_1)x^k}{k![(n_1+1)\mu_1]^{p_1+m_1-k}\bar{\rho}_A^k a_1^k} \\ &\quad + \sum_{k=0}^{p_1+m_1-1} \frac{\Gamma(p_1+m_1)x^k \rho_Q^{p_0+m_0} a_1^{p_0+m_0}}{k![(n_1+1)\mu_1]^{p_1+m_1-k}} \\ &\quad \left. \times \frac{\Gamma\left(p_0+m_0+k, \bar{\rho}_A^{-1}\rho_Q\left[(n_0+1)\mu_0 + \frac{(n_1+1)\mu_1 x}{\rho_Q a_1}\right]\right)}{\left[\rho_Q a_1(n_0+1)\mu_0 + (n_1+1)\mu_1 x\right]^{p_0+m_0+k}} \right\}. \end{aligned} \tag{58}$$

Substituting (58) into (56) and after some steps, this can yield to result in (59), shown at the top of the next page, where step (a) follows by letting $t = (4/\pi)\arctan(x) - 1$; step (b) follows by using the Gaussian–Chebyshev quadrature approximation [42]; C is a parameter which determines the tradeoff between complexity and accuracy; $\xi_c = \cos([2u - 1/2C]\pi)$.

Then, the EC of U_1 in case of pSIC can be obtained as (59).

$$\begin{aligned} \mathcal{V}_1 &= \int_0^{\frac{\rho_Q}{\bar{\rho}_A}} f_{\hat{Z}_0^*}(y) \int_0^{\infty} f_{|g_I|^2}(z) \int_{x\left(\frac{z}{a_1}+\frac{1}{\bar{\rho}_A a_1}\right)}^{\infty} f_{\hat{Z}_1^*}(w) dydzdw \\ &= \frac{\mathcal{G}(N, n_0, m_0, p_0)\mathcal{G}(N, n_1, m_1, p_1)}{\lambda_I} \int_0^{\frac{\rho_Q}{\bar{\rho}_R}} y^{p_0+m_0-1} e^{-(n_0+1)\mu_0 y} \int_0^{\infty} e^{-\frac{z}{\lambda_I}} \int_{x\left(\frac{z}{a_1}+\frac{1}{\bar{\rho}_R a_1}\right)}^{\infty} w^{p_1+m_1-1} e^{-(n_1+1)\mu_1 w} dydzdw \\ &= e^{-\frac{(n_1+1)\mu_1}{\bar{\rho}_A a_1}x} \frac{\mathcal{G}(N, n_0, m_0, p_0)\mathcal{G}(N, n_1, m_1, p_1)\gamma\left(p_0+m_0, \rho_Q\bar{\rho}_A^{-1}(n_0+1)\mu_0\right)}{\lambda_I[(n_0+1)\mu_0]^{p_0+m_0}} \sum_{k=0}^{p_1+m_1-1} \frac{\Gamma(p_1+m_1)x^k}{k![(n_1+1)\mu_1]^{p_1+m_1-k}} \\ &\quad \times \int_0^{\infty} \left(\frac{z}{a_1} + \frac{1}{\bar{\rho}_A a_1}\right)^k e^{-\left[\frac{1}{\lambda_I} + \frac{x(n_1+1)\mu_1}{a_1}\right]z} dz \end{aligned} \tag{52a}$$

$$\begin{aligned} \mathcal{V}_2 &= \int_{\frac{\rho_Q}{\bar{\rho}_A}}^{\infty} f_{\hat{Z}_0^*}(y) \int_0^{\infty} f_{|g_I|^2}(z) \int_{x\left(\frac{z}{a_1}+\frac{y}{\rho_Q a_1}\right)}^{\infty} f_{\hat{Z}_1^*}(w) dydzdw \\ &= \frac{\mathcal{G}(N, n_0, m_0, p_0)\mathcal{G}(N, n_1, m_1, p_1)}{\lambda_I} \int_{\frac{\rho_Q}{\bar{\rho}_R}}^{\infty} y^{p_0+m_0-1} e^{-(n_0+1)\mu_0 y} \int_0^{\infty} e^{-\frac{z}{\lambda_I}} \int_{x\left(\frac{z}{a_1}+\frac{y}{\rho_Q a_1}\right)}^{\infty} w^{p_1+m_1-1} e^{-(n_1+1)\mu_1 w} dydzdw \\ &= \frac{\mathcal{G}(N, n_0, m_0, p_0)\mathcal{G}(N, n_1, m_1, p_1)}{\lambda_I} \sum_{k=0}^{p_1+m_1-1} \frac{\Gamma(p_1+m_1)x^k}{k![(n_1+1)\mu_1]^{p_1+m_1-k}a_1^k} \\ &\quad \times \int_{\frac{\rho_Q}{\bar{\rho}_A}}^{\infty} y^{p_0+m_0-1} e^{-\left[(n_0+1)\mu_0 + \frac{(n_1+1)\mu_1 x}{\rho_Q a_1}\right]y} \int_0^{\infty} e^{-\left[\frac{1}{\lambda_I} + \frac{(n_1+1)\mu_1 x}{a_1}\right]z} \left(z + \rho_Q^{-1} y\right)^k dydz \end{aligned} \tag{52b}$$

$$\begin{aligned} \mathcal{V}_1 &= \mathcal{G}(N, n_0, m_0, p_0)\mathcal{G}(N, n_1, m_1, p_1) \frac{\gamma\left(p_0+m_0, \rho_Q\bar{\rho}_A^{-1}(n_0+1)\mu_0\right)}{[(n_0+1)\mu_0]^{p_0+m_0}} \sum_{k=0}^{p_1+m_1-1} \sum_{v=0}^{k} \binom{k}{v} \frac{v!\Gamma(p_1+m_1)\lambda_I^v a_1^{v-k+1}}{k![(n_1+1)\mu_1]^{p_1+m_1-k}\bar{\rho}_A^{k-v}} \\ &\quad \times \frac{x^k e^{-\frac{(n_1+1)\mu_1}{\bar{\rho}_A a_1}x}}{[a_1 + x\lambda_I(n_1+1)\mu_1]^{v+1}} \end{aligned} \tag{53a}$$

$$\begin{aligned} \mathcal{V}_2 &= \mathcal{G}(N, n_0, m_0, p_0)\mathcal{G}(N, n_1, m_1, p_1) \sum_{k=0}^{p_1+m_1-1} \sum_{v=0}^{k} \binom{k}{v} \frac{\Gamma(p_1+m_1)(k-v)!a_1^{p_0+m_0+1}\rho_Q^{p_0+m_0}\lambda_I^{k-v}x^k}{k![(n_1+1)\mu_1]^{p_1+m_1-k}[a_1 + x\lambda_I(n_1+1)\mu_1]^{k-v+1}} \\ &\quad \times \frac{\Gamma\left(p_0+m_0+v, \rho_Q\bar{\rho}_A^{-1}\left[(n_0+1)\mu_0 + \frac{x(n_1+1)\mu_1}{\rho_Q a_1}\right]\right)}{\left[\rho_Q a_1(n_0+1)\mu_0 + x(n_1+1)\mu_1\right]^{p_0+m_0+v}} \end{aligned} \tag{53b}$$

$$\mathcal{C}_1^{\text{ipSIC}} = \frac{1}{2\ln 2}\int_0^{\infty}\frac{1}{1+x}\mathcal{G}(N,n_0,m_0,p_0)\mathcal{G}(N,n_1,m_1,p_1)\Bigg\{\frac{\gamma\Big(p_0+m_0,\rho_Q\bar{\rho}_A^{-1}(n_0+1)\mu_0\Big)}{[(n_0+1)\mu_0]^{p_0+m_0}}$$
$$\times\sum_{k=0}^{p_1+m_1-1}\sum_{v=0}^{k}\binom{k}{v}\frac{v!\Gamma(p_1+m_1)\lambda_I^v a_1^{v-k+1}x^k e^{-\frac{(n_1+1)\mu_1}{\bar{\rho}_A a_1}x}}{k![(n_1+1)\mu_1]^{p_1+m_1-k}[a_1+x\lambda_I(n_1+1)\mu_1]^{v+1}\bar{\rho}_A^{k-v}}+\sum_{k=0}^{p_1+m_1-1}\sum_{v=0}^{k}\binom{k}{v}\frac{\Gamma(p_1+m_1)(k-v)!}{k![(n_1+1)\mu_1]^{p_1+m_1-k}}$$
$$\times\frac{a_1^{p_0+m_0+1}\rho_Q^{p_0+m_0}\lambda_I^{k-v}x^k\Gamma\Big(p_0+m_0+v,\rho_Q\bar{\rho}_A^{-1}\Big[(n_0+1)\mu_0+\rho_Q^{-1}a_1^{-1}x(n_1+1)\mu_1\Big]\Big)}{[a_1+x\lambda_I(n_1+1)\mu_1]^{k-v+1}\Big[\rho_Q a_1(n_0+1)\mu_0+x(n_1+1)\mu_1\Big]^{p_0+m_0+v}}\Bigg\}dx$$
$$=\frac{\pi}{8\ln 2}\int_{-1}^{1}\frac{1}{1+g(t)}\sec^2\Big(\frac{\pi}{4}(t+1)\Big)\mathcal{G}(N,n_0,m_0,p_0)\mathcal{G}(N,n_1,m_1,p_1)\Bigg\{\frac{\gamma\Big(p_0+m_0,\rho_Q\bar{\rho}_A^{-1}(n_0+1)\mu_0\Big)}{[(n_0+1)\mu_0]^{p_0+m_0}}$$
$$\times\sum_{k=0}^{p_1+m_1-1}\sum_{v=0}^{k}\binom{k}{v}\frac{v!\Gamma(p_1+m_1)\lambda_I^v a_1^{v-k+1}g(t)^k e^{-\frac{(n_1+1)\mu_1}{\bar{\rho}_A a_1}g(t)}}{k![(n_1+1)\mu_1]^{p_1+m_1-k}\big[a_1+g(t)\lambda_I(n_1+1)\mu_1\big]^{v+1}\bar{\rho}_A^{k-v}}+\sum_{k=0}^{p_1+m_1-1}\sum_{v=0}^{k}\binom{k}{v}\frac{\Gamma(p_1+m_1)(k-v)!}{k![(n_1+1)\mu_1]^{p_1+m_1-k}}$$
$$\times\frac{a_1^{p_0+m_0+1}\rho_Q^{p_0+m_0}\lambda_I^{k-v}g(t)^k\Gamma\Big(p_0+m_0+v,\rho_Q\bar{\rho}_A^{-1}\Big[(n_0+1)\mu_0+\rho_Q^{-1}a_1^{-1}g(t)(n_1+1)\mu_1\Big]\Big)}{\big[a_1+g(t)\lambda_I(n_1+1)\mu_1\big]^{k-v+1}\big[\rho_Q a_1(n_0+1)\mu_0+g(t)(n_1+1)\mu_1\big]^{p_0+m_0+v}}\Bigg\}dt \tag{54}$$

$$\mathcal{C}_1^{\text{ipSIC}}\approx\frac{\pi^2}{8U\ln 2}\sum_{u=1}^{U}\frac{\sqrt{1-\xi_u^2}}{1+g(\xi_u)}\sec^2\Big(\frac{\pi}{4}(\xi_u+1)\Big)\mathcal{G}(N,n_0,m_0,p_0)\mathcal{G}(N,n_1,m_1,p_1)\Bigg\{\frac{\gamma\Big(p_0+m_0,\rho_Q\bar{\rho}_A^{-1}(n_0+1)\mu_0\Big)}{[(n_0+1)\mu_0]^{p_0+m_0}}\sum_{k=0}^{p_1+m_1-1}\sum_{v=0}^{k}\binom{k}{v}$$
$$\times\frac{v!\Gamma(p_1+m_1)\lambda_I^v a_1^{v-k+1}g(\xi_u)^k e^{-\frac{(n_1+1)\mu_1}{\bar{\rho}_A a_1}g(\xi_u)}}{k![(n_1+1)\mu_1]^{p_1+m_1-k}\big[a_1+g(\xi_u)\lambda_I(n_1+1)\mu_1\big]^{v+1}\bar{\rho}_A^{k-v}}+\sum_{k=0}^{p_1+m_1-1}\sum_{v=0}^{k}\binom{k}{v}\frac{\Gamma(p_1+m_1)(k-v)!a_1^{p_0+m_0+1}}{k!\big[a_1+g(\xi_u)\lambda_I(n_1+1)\mu_1\big]^{k-v+1}}$$
$$\times\frac{\rho_Q^{p_0+m_0}\lambda_I^{k-v}g(\xi_u)^k\Gamma\Big(p_0+m_0+v,\rho_Q\bar{\rho}_A^{-1}\Big[(n_0+1)\mu_0+\big(\rho_Q a_1\big)^{-1}g(\xi_u)(n_1+1)\mu_1\Big]\Big)}{[(n_1+1)\mu_1]^{p_1+m_1-k}\big[\rho_Q a_1(n_0+1)\mu_0+g(\xi_u)(n_1+1)\mu_1\big]^{p_0+m_0+v}}\Bigg\} \tag{55}$$

$$\mathcal{C}_1^{\text{pSIC}}\overset{(a)}{=}\frac{\pi}{8\ln 2}\int_{-1}^{1}\frac{\sec^2\big(\frac{\pi}{4}(t+1)\big)}{1+g(t)}\mathcal{G}(N,n_0,m_0,p_0)\mathcal{G}(N,n_1,m_1,p_1)\Bigg\{\frac{e^{-\frac{(n_1+1)\mu_1 g(t)}{\bar{\rho}_A a_1}}\gamma\Big(p_0+m_0,\bar{\rho}_A^{-1}\rho_Q(n_0+1)\mu_0\Big)}{[(n_0+1)\mu_0]^{p_0+m_0}}\sum_{k=0}^{p_1+m_1-1}\frac{g(t)^k}{k!\bar{\rho}_A^k a_1^k}$$
$$\times\frac{\Gamma(p_1+m_1)}{[(n_1+1)\mu_1]^{p_1+m_1-k}}+\sum_{k=0}^{p_1+m_1-1}\frac{\Gamma(p_1+m_1)g(t)^k\rho_Q^{p_0+m_0}a_1^{p_0+m_0}}{k![(n_1+1)\mu_1]^{p_1+m_1-k}}\frac{\Gamma\Big(p_0+m_0+k,\bar{\rho}_A^{-1}\rho_Q\Big[(n_0+1)\mu_0+\rho_Q^{-1}a_1^{-1}(n_1+1)\mu_1 g(t)\Big]\Big)}{\big[\rho_Q a_1(n_0+1)\mu_0+(n_1+1)\mu_1 g(t)\big]^{p_0+m_0+k}}\Bigg\}dt$$
$$\overset{(b)}{\approx}\frac{\pi^2}{8C\ln 2}\sum_{c=1}^{C}\frac{\sqrt{1-\xi_c^2}}{1+g(\xi_c)}\sec^2\Big(\frac{\pi}{4}(\xi_c+1)\Big)\mathcal{G}(N,n_0,m_0,p_0)\mathcal{G}(N,n_1,m_1,p_1)\Bigg\{\frac{\gamma\Big(p_0+m_0,\bar{\rho}_A^{-1}\rho_Q(n_0+1)\mu_0\Big)}{[(n_0+1)\mu_0]^{p_0+m_0}}e^{-\frac{(n_1+1)\mu_1 g(\xi_c)}{\bar{\rho}_A a_1}}$$
$$\times\sum_{k=0}^{p_1+m_1-1}\frac{\Gamma(p_1+m_1)g(\xi_c)^k}{k![(n_1+1)\mu_1]^{p_1+m_1-k}\bar{\rho}_A^k a_1^k}+\sum_{k=0}^{p_1+m_1-1}\frac{\Gamma(p_1+m_1)g(\xi_c)^k\rho_Q^{p_0+m_0}a_1^{p_0+m_0}}{k![(n_1+1)\mu_1]^{p_1+m_1-k}\big[\rho_Q a_1(n_0+1)\mu_0+(n_1+1)\mu_1 g(\xi_c)\big]^{p_0+m_0+k}}$$
$$\times\Gamma\Big(p_0+m_0+k,\bar{\rho}_A^{-1}\rho_Q\Big[(n_0+1)\mu_0+\rho_Q^{-1}a_1^{-1}(n_1+1)\mu_1 g(\xi_c)\Big]\Big)\Bigg\} \tag{59}$$

This completes the proof.

REFERENCES

[1] Y. Xu, G. Gui, H. Gacanin, and F. Adachi, "A survey on resource allocation for 5G heterogeneous networks: Current research, future trends, and challenges," *IEEE Commun. Surveys Tuts.*, vol. 23, no. 2, pp. 668–695, 2nd Quart., 2021.

[2] S. Shakoor, Z. Kaleem, D.-T. Do, O. A. Dobre, and A. Jamalipour, "Joint optimization of UAV 3D placement and path loss factor for energy efficient maximal coverage," *IEEE Internet Things J.*, vol. 8, no. 12, pp. 9776–9786, Jun. 2021.

[3] B. Ji, Y. Li, S. Chen, C. Han, C. Li, and H. Wen, "Secrecy outage analysis of UAV assisted relay and antenna selection for cognitive network under Nakagami-*m* channel," *IEEE Trans. Cogn. Commun. Netw.*, vol. 6, no. 3, pp. 904–914, Sep. 2020.

[4] Z. Wang and L. Duan, "Chase or wait: Dynamic UAV deployment to learn and catch time-varying user activities," *IEEE Trans. Mobile Comput.*, early access, Aug. 24, 2021, doi: 10.1109/TMC.2021.3107027.

[5] M.-S. Van Nguyen, D.-T. Do, S. Al-Rubaye, S. Mumtaz, A. Al-Dulaimi, and O. Dobre, "Exploiting impacts of antenna selection and energy harvesting for massive network connectivity," *IEEE Trans. Commun.*, vol. 69, no. 11, pp. 7587–7602, Nov. 2021.

[6] Z. Ding, R. Schober, and H. V. Poor, "Unveiling the importance of SIC in NOMA systems—Part 1: State of the art and recent findings," *IEEE Commun. Lett.*, vol. 24, no. 11, pp. 2373–2377, Nov. 2020.

[7] W. Shi et al., "Joint UL/DL resource allocation for UAV-aided full-duplex NOMA communications," *IEEE Trans. Commun.*, vol. 69, no. 12, pp. 8474–8487, Dec. 2021.
[8] T.-H. Vu, T.-V. Nguyen, and S. Kim, "Wireless powered cognitive NOMA-based IoT relay networks: Performance analysis and deep learning evaluation," *IEEE Internet Things J.*, vol. 9, no. 5, pp. 3913–3929, Mar. 2022.
[9] L. Sboui, H. Ghazzai, Z. Rezki, and M. Alouini, "Energy-efficient power allocation for UAV cognitive radio systems," in *Proc. IEEE 86th Veh. Technol. Conf. (VTC-Fall)*, 2017, pp. 1–5.
[10] X. Zheng, J. Zhang, and G. Pan, "On secrecy analysis of underlay cognitive UAV-aided NOMA systems with TAS/MRC," *IEEE Internet Things J.*, vol. 9, no. 22, pp. 22631–22642, Nov. 2022, doi: 10.1109/JIOT.2022.3181826.
[11] Y. Pan, X. Da, H. Hu, Z. Zhu, R. Xu, and L. Ni, "Energy-efficiency optimization of UAV-based cognitive radio system," *IEEE Access*, vol. 7, pp. 155381–155391, 2019.
[12] H. Hu, Y. Huang, X. Da, H. Zhang, L. Ni, and Y. Pan, "Optimization of energy management for UAV-enabled cognitive radio," *IEEE Wireless Commun. Lett.*, vol. 9, no. 9, pp. 1505–1508, Sep. 2020.
[13] Y. Wang, L. Chen, Y. Zhou, X. Liu, F. Zhou, and N. Al-Dhahir, "Resource allocation and trajectory design in UAV-assisted jamming wideband cognitive radio networks," *IEEE Trans. Cogn. Commun. Netw.*, vol. 7, no. 2, pp. 635–647, Jun. 2021.
[14] X. He, X. Li, H. Ji, and H. Zhang, "Resource allocation for secrecy rate optimization in UAV-assisted cognitive radio network," in *Proc. IEEE Wireless Commun. Netw. Conf. (WCNC)*, 2021, pp. 1–6.
[15] X. Sun, W. Yang, and Y. Cai, "Secure communication in NOMA-assisted millimeter-wave SWIPT UAV networks," *IEEE Internet Things J.*, vol. 7, no. 3, pp. 1884–1897, Mar. 2020.
[16] D.-T. Do, A.-T. Le, Y. Liu, and A. Jamalipour, "User grouping and energy harvesting in UAV-NOMA system with AF/DF relaying," *IEEE Trans. Veh. Technol.*, vol. 70, no. 11, pp. 11855–11868, Nov. 2021.
[17] C. K. Singh and P. K. Upadhyay, "Overlay cognitive IoT-based full-duplex relaying NOMA systems with hardware imperfections," *IEEE Internet Things J.*, vol. 9, no. 9, pp. 6578–6596, May 2022.
[18] T. Z. H. Ernest, A. S. Madhukumar, R. P. Sirigina, and A. K. Krishna, "NOMA-aided UAV communications over correlated rician shadowed fading channels," *IEEE Trans. Signal Process.*, vol. 68, pp. 3103–3116, May 2020.
[19] S. Arzykulov, A. Celik, G. Nauryzbayev, and A. M. Eltawil, "UAV-assisted cooperative cognitive NOMA: Deployment, clustering, and resource allocation," *IEEE Trans. Cogn. Commun. Netw.*, vol. 8, no. 1, pp. 263–281, Mar. 2022, doi: 10.1109/TCCN.2021.3105133.
[20] X. Liu, H. Ding, and S. Hu, "Uplink resource allocation for NOMA-based hybrid spectrum access in 6G-enabled cognitive Internet of Things," *IEEE Internet Things J.*, vol. 8, no. 20, pp. 15049–15058, Oct. 2021.
[21] M. Wu, Q. Song, L. Guo, and A. Jamalipour, "Joint user pairing and resource allocation in a SWIPT-enabled cooperative NOMA system," *IEEE Trans. Veh. Technol.*, vol. 70, no. 7, pp. 6826–6840, Jul. 2021.
[22] A. A. Khuwaja, Y. Chen, and G. Zheng, "Effect of user mobility and channel fading on the outage performance of UAV communications," *IEEE Wireless Commun. Lett.*, vol. 9, no. 3, pp. 367–370, Mar. 2020.
[23] A. Bhowmick, S. D. Roy, and S. Kundu, "Throughput maximization of a UAV assisted CR network with NOMA-based communication and energy-harvesting," *IEEE Trans. Veh. Technol.*, vol. 71, no. 1, pp. 362–374, Jan. 2022.
[24] A. Vahid, M. A. Maddah-Ali, and S. Avestimehr, "Capacity results for binary fading interference channels with delayed CSIT," *IEEE Trans. Inf. Theory*, vol. 60, no. 10, pp. 6093–6130, Oct. 2014.
[25] A. Vahid, M. A. Maddah-Ali, and S. Avestimehr, "Approximate capacity region of the MISO broadcast channels with delayed CSIT," *IEEE Trans. Commun.*, vol. 64, no. 7, pp. 2913–2924, Jun. 2016.
[26] A. Vahid and R. Calderbank, "Two-user erasure interference channels with local delayed CSIT," *IEEE Trans. Inf. Theory*, vol. 62, no. 9, pp. 4910–4923, Sep. 2016.
[27] A. Vahid, V. Aggarwal, S. Avestimehr, and A. Sabharwal, "Interference management with mismatched partial channel state information," *EURASIP J. Wireless Commun. Netw.*, vol. 2017, no. 1, pp. 1–22, 2017.
[28] S. C. Lin, I. H. Wang, and A. Vahid, "Capacity of broadcast packet erasure channels with single-user delayed CSI," *IEEE Trans. Inf. Theory*, vol. 67, no. 10, pp. 6283–6295, Oct. 2021.
[29] A. Vahid, S.-C. Lin, and I.-H. Wang, "Erasure broadcast channels with intermittent feedback," *IEEE Trans. Commun.*, vol. 69, no. 11, pp. 7363–7375, Nov. 2021.
[30] B. Ji, Y. Li, D. Cao, C. Li, S. Mumtaz, and D. Wang, "Secrecy performance analysis of UAV assisted relay transmission for cognitive network with energy harvesting," *IEEE Trans. Veh. Technol.*, vol. 69, no. 7, pp. 7404–7415, Jul. 2020.
[31] J. Ye, C. Zhang, H. Lei, G. Pan, and Z. Ding, "Secure UAV-to-UAV systems with spatially random UAVs," *IEEE Wireless Commun. Lett.*, vol. 8, no. 2, pp. 564–567, Apr. 2019.
[32] T. N. Do, D. B. da Costa, T. Q. Duong, and B. An, "Improving the performance of cell-edge users in MISO-NOMA systems using TAS and SWIPT-based cooperative transmissions," *IEEE Trans. Green Commun. Netw.*, vol. 2, no. 1, pp. 49–61, Mar. 2018.
[33] M. F. Kader, M. B. Shahab, and S. Y. Shin, "Exploiting non-orthogonal multiple access in cooperative relay sharing," *IEEE Commun. Lett.*, vol. 21, no. 5, pp. 1159–1162, May 2017.
[34] Y. Xu et al., "Coordinated direct and relay transmission with NOMA and network coding in Nakagami-*m* fading channels," *IEEE Trans. Commun.*, vol. 69, no. 1, pp. 207–222, Jan. 2021.
[35] J. Men, J. Ge, and C. Zhang, "Performance analysis for downlink relaying aided non-orthogonal multiple access networks with imperfect CSI over Nakagami-*m* fading," *IEEE Access*, vol. 5, pp. 998–1004, 2016.
[36] I. S. Gradshteyn and I. M. Ryzhik, *Tables of Integrals, Series and Products*. 6th ed. New York, NY, USA: Academic, 2000.
[37] R. Zhao, Y. Yuan, L. Fan, and Y.-C. He, "Secrecy performance analysis of cognitive decode-and-forward relay networks in Nakagami-*m* fading channels,"*IEEE Trans. Commun.*, vol. 65, no. 2, pp. 549–563, Feb. 2017.
[38] A. Annamalai and C. Tellambura, "Error rates for Nakagami-*m* fading multi channel reception of binary and M-ary signals," *IEEE Trans. Commun.*, vol. 49, no. 1, pp. 58–68, Jan. 2001.
[39] X. Li et al., "Physical layer security of cognitive ambient backscatter communications for green Internet of Things," *IEEE Trans. Green Commun. Netw.*, vol. 5, no. 3, pp. 1066–1076, Sep. 2021.
[40] Y. Cheng, K. H. Li, Y. Liu, K. C. Teh, and H. V. Poor, "Downlink and uplink intelligent reflecting surface aided networks: NOMA and OMA," *IEEE Trans. Wireless Commun.*, vol. 20, no. 6, pp. 3988–4000, Jun. 2021.
[41] Q. Wang, X. Li, Y. Liu, L. T. Alex, S. A. Khowaja, and V. G. Menon, "UAV-enabled non-orthogonal multiple access networks for ground-air-ground communications," *IEEE Trans. Green Commun. Netw.*, vol. 6, no. 3, pp. 1340–1354, Sep. 2022.
[42] M. Abramowitz and I. A. Stegun, *Handbook of Mathematical Functions With Formulas, Graphs, and Mathematical Tables*. New York, NY, USA: Dover, 1972.

Dinh-Thuan Do (Senior Member, IEEE) received the B.S., M.Eng., and Ph.D. degrees in communications engineering from Viet Nam National University (VNU-HCMC), Hanoi, Vietnam, in 2003, 2007, and 2013, respectively.

Before joining the University of Colorado Denver, Denver, Colorado, as a Postdoctoral Fellow in 2022, he worked as a Research Scientist with The University of Texas at Austin, Austin, TX, USA, in 2021, and an Assistant Professor with Asia University, Taichung, Taiwan, from 2020 to 2021. He published one textbook and five edited books. He has authored or coauthored over 100 technical papers published in peer-reviewed international journals (SCIE). His research interest includes signal processing in wireless communications network, reconfigurable intelligent surfaces, NOMA, UAV network, satellite system, physical-layer security, device-to-device transmission, and energy harvesting.

Dr. Thuan was a recipient of the Golden Globe Award from Vietnam Ministry of Science and Technology in 2015 (Top 10 talented young scientists nationwide). He got the Creative Young Medal in 2015. He was named in top list of 14 Highly Cited Scientists at Asia University in 2021. He led as a lead guest editor/guest editor in more than 15 special issues in peer-reviewed journals. He is serving as an Associate Editor in IEEE TRANSACTIONS ON VEHICULAR TECHNOLOGY and *Computer Communications*.

Chi-bao Le was born in Binh Thuan, Vietnam. He is currently pursuing the master's degree in wireless communications.

He worked closely with Dr. Thuan at the Wireless Communications and Signal Processing Research Group, Industrial University of Ho Chi Minh City, Ho Chi Minh City, Vietnam. His research interests include signal processing in wireless communications networks, nonorthogonal multiple access, and physical-layer security.

Alireza Vahid (Senior Member, IEEE) received the B.Sc. degree in electrical engineering from the Sharif University of Technology, Tehran, Iran, in 2009, and the M.Sc. and Ph.D. degrees in electrical and computer engineering from Cornell University, Ithaca, NY, USA, in 2012 and 2015, respectively.

From 2015 to 2017, he worked as a Postdoctoral Research Scientist with the Information Initiative, Duke University, Durham, NC, USA. He is currently an Assistant Professor of Electrical Engineering with the University of Colorado at Denver, Denver, CO, USA. His research interests include network information theory, wireless communications, coding theory, and applications of coding theory in high-performance computer memory systems.

Dr. Vahid received the 2015 Outstanding Ph.D. Thesis Research Award, the 2010 Director's Ph.D. Teaching Award, the Jacobs Scholar Fellowship in 2009 from Cornell University, the 2013 Qualcomm Innovation Fellowship, the 2019 Lab Venture Challenge Award, and the 2021 SONY Faculty Innovation Award. He currently serves as an Associate Editor for IEEE COMMUNICATIONS LETTERS.

Shahid Mumtaz (Senior Member, IEEE) received the master's degree from Blekinge Institute of Technology, Karlskrona, Sweden, in 2005, and the Ph.D. degree from the University of Aveiro, Aveiro, Portugal, in 2011.

He has authored four technical books, 12 book chapters, more than 300 technical papers, more than 200 IEEE Journals/transactions, and more than 100 conferences. Most of his publication is in the field of wireless communication.

Dr. Mumtaz is the recipient of the NSFC Researcher Fund for Young Scientist in 2017 from China and the IEEE ComSoC Young Researcher Award in 2020. He was awarded an Alain Bensoussan Fellowship in 2012. He received two IEEE Best Paper Awards in the area of mobile communications. He is the Founder and the EiC of *IET Journal of Quantum Communication*, a Vice Chair of Europe/Africa Region—IEEE ComSoc: Green Communications & Computing society and the IEEE standard on P1932.1: Standard for Licensed/Unlicensed Spectrum Interoperability in Wireless Mobile Networks. He is serving as the Scientific Expert and the Evaluator for various Research Funding Agencies. He is an IET Fellow, the IEEE ComSoc Lecturer, and an ACM Distinguished Speaker.